Investigating the dispersion behavior in solvents, biocompatibility and use as support for highly efficient metal catalysts of exfoliated graphitic carbon nitride

M. Ayán–Varela,[a] S. Villar–Rodil,[a,*] J.I. Paredes,[a] J.M. Munuera,[a] A. Pagán,[b] A. A. Lozano–Pérez,[b] J.L. Cenis,[b] A. Martínez–Alonso,[a] J.M.D. Tascón[a]

[a]Instituto Nacional del Carbón, INCAR-CSIC, Apartado 73, 33080 Oviedo, Spain

[b]Instituto Murciano de Investigación y Desarrollo Agrario y Alimentario (IMIDA), C/ Mayor 1, 30150 La Alberca (Murcia), Spain

*Corresponding author: E-mail address: silvia@incar.csic.es (S. Villar-Rodil)

Abstract
The liquid-phase exfoliation of graphitic carbon nitride (g-C_3N_4) to afford colloidal dispersions of two-dimensional flakes constitutes an attractive route to facilitate the processing and implementation of this novel material towards different technological applications, but quantitative knowledge about its dispersibility in solvents is lacking. Here, we investigate the dispersion behavior of exfoliated g-C_3N_4 in a wide range of solvents and evaluate the obtained results on the basis of solvent surface energy and Hildebrand/Hansen solubility parameters. Estimates of the three Hansen parameters for exfoliated g-C_3N_4 from the experimentally derived data yielded yielded $\delta_D \approx 17.8$ $MPa^{1/2}$, $\delta_P \approx 10.8$ $MPa^{1/2}$ and $\delta_H \approx 15.4$ $MPa^{1/2}$. The relatively high δ_H value suggested that, contrary to the case of other two-dimensional materials (e.g., graphene or transition metal dichalcogenides), hydrogen-bonding plays a substantial role in the efficient interaction, and thus dispersibility, of exfoliated g-C_3N_4 with solvents. Such an outcome was attributed to a high density of primary and/or secondary amines in the material, the presence of which was associated to incomplete condensation of the structure. Furthermore, cell proliferation tests carried out on thin films of exfoliated g-C_3N_4 using murine fibroblasts suggested that this material is highly biocompatible and non-cytotoxic. Finally, the exfoliated g-C_3N_4 flakes were used as supports in the synthesis of Pd nanoparticles, and the resulting hybrids exhibited an exceptional catalytic activity in the reduction of nitroarenes.

Keywords: graphitic carbon nitride, colloidal dispersion, graphitic hybrid materials, metal nanoparticles, catalytic reduction

1 Introduction

The isolation of graphene in 2004 and the subsequent discovery of its exceptional physical properties[1,2] have aroused in more recent years great research interest in two-dimensional (2D) materials in general.[3] The reduced dimensionality of 2D materials introduces unique electronic, mechanical or optical properties that are frequently absent from their bulk counterparts, making them promising candidates for many applications in different fields, such as electronics, photonics, chemical sensing and biosensing, energy conversion and storage or catalysis.[4] Indeed, there is currently enormous interest in the development of a plethora of 2D materials, including transition metal dichalcogenides, transition metal oxides or hexagonal boron nitride, with novel and interesting properties. In this context, top-down approaches involving exfoliation of the parent layered material are one of the most useful strategies towards their mass preparation, a prerequisite for their large-scale practical implementation.[5] Particularly, methods based on the exfoliation of layered materials in the liquid phase to yield colloidal dispersions of 2D nanosheets are very much sought after, as they boast a number of advantages.[6] Apart from potentially affording scalable production of the nanosheets, such methods facilitate their chemical modification by wet techniques and their processing into different macroscopic materials, such as thin films, composites or hybrid materials.

Recently, graphitic carbon nitride (g–C_3N_4), a polymeric semiconductor that is the most stable allotrope of carbon nitride,[7] has become the focus of significant attention amongst layered materials due to its prospective application in many relevant technological fields, such as catalysis, photocatalysis, energy conversion, chemical sensing and biosensing, or biomedicine.[8–17]. g–C_3N_4 possesses a graphite-like layered structure based on 2D sheets of tris-*s*-triazine units connected by tertiary amines as

basic building block,[7] as shown in Fig. 1, and is commonly synthesized by polycondensation of nitrogen-rich organic precursors (e.g., cyanamide, melamine or urea).[7, 18, 19] This layered material possesses high chemical and thermal stability, withstanding mild acids, bases and organic solvents[20] as well as temperatures up to 600 ºC in air[17] without significant degradation. However, g–C_3N_4 in bulk form exhibits several features that limit its use in many of its most relevant potential applications, such as low specific surface area, high recombination rate of photogenerated charges,[21,22] and a medium-scale bandgap. Some strategies have been attempted to overcome these disadvantages, such as doping with heteroatoms,[23,24] controlling its nanometer-scale morphology or structure,[25,26] or combining it with other materials to form composites,[27,28] or hybrids.[29] As recent theoretical studies have predicted, and in line with what is usually observed for other layered materials, exfoliation of g–C_3N_4 to yield 2D nanosheets should also lead to improved and/or emerging properties compared with its bulk counterpart.[30] For instance, the probability of recombination of photogenerated charge carriers is reduced, the bandgap enlarged, the specific surface area increased and the catalytic activity improved when g–C_3N_4 is exfoliated into thin nanosheets.[31,32]

Similar to the case of graphene and other 2D materials,[33,34,35], amongst the possible methods to obtain g–C_3N_4 nanosheets[31–41] exfoliation in the liquid phase assisted by sonication [37] to give colloidal dispersions is particularly attractive, as it introduces little or no chemical and structural modification to the material, making it the production method of choice towards many purposes. However, at present only a few studies on the liquid-phase exfoliation and colloidal dispersion of g–C_3N_4 have been reported in the literature, being mostly qualitative in nature and limited to a reduced number of solvents.[37, 42 – 45] Owing to the practical relevance of exfoliated g–C_3N_4, a more quantitative and comprehensive knowledge of its colloidal dispersibility, in the vein of that previously attained for different types of graphene as well as other 2D materials, would be highly desirable, as this would facilitate its manipulation and processing towards many different potential applications.

Here we report a quantitative study on the dispersion behavior of exfoliated g–C_3N_4 in a wide range of solvents, evaluated on the basis of their surface energy and Hildebrand/Hansen solubility parameters. As could be expected from the singular characteristics of g–C_3N_4, which will be discussed below, the colloidal dispersion behavior of this material turned out to be complex and differed from that previously reported for other 2D materials, (e.g., graphene and transition metal dichalcogenides). We also demonstrate that the exfoliated g–C_3N_4 nanosheets are excellent supports for the growth of noble metal (Pd) nanoparticles (NPs) and the resulting g–C_3N_4–Pd NP hybrids possess an exceptional catalytic activity, as demonstrated by the reduction of 4-nitrophenol (4–NP) and 4-nitroaniline (4–NA) with $NaBH_4$ taken as model reactions. Finally, g–C_3N_4 is generally thought to be a biocompatible substance with potential use in biomedicine, but to the best of our knowledge no biocompatibility studies have yet been reported for materials based on exfoliated g–C_3N_4. As an initial biocompatibility assessment, we also describe here the culture of the murine fibroblast cell line L–929 on thin films of exfoliated g–C_3N_4, the results suggesting that the material lacks significant cytotoxicity.

2 Experimental section

2.1 Exfoliation and dispersion behavior of g–C_3N_4 in solvents

A commercial g–C_3N_4 powder obtained from Carbodeon Ltd. (chemical purity ≥99.5%, particle size >30 μm) was used as starting material. All the solvents were provided by Sigma-Aldrich and used as received. The effect of different processing parameters on the liquid-phase exfoliation and dispersion of g-C_3N_4 was investigated, but the typical procedure employed for every g–C_3N_4/solvent combination was as follows: 30 mg of g–C_3N_4 was added to 10 mL of the corresponding solvent, the mixture was sonicated for 4 hours at a power of 20 W L^{-1} in an ultrasound bath cleaner (JP Selecta Ultrasons system, 40 kHz), subsequently centrifuged at 500*g* for 10 min (Eppendorf 5424 microcentrifugue), and finally the top ~75% of the resulting supernatant volume was collected for further analysis. To quantitatively assess the efficiency of each solvent to exfoliate and colloidally stabilize g-C_3N_4, we estimated the amount of material in dispersion by measuring its optical absorbance through a double beam Heλios α spectrophotometer (Thermo Spectronic). The measured absorbance is known to be proportional to the dispersed concentration according to the Lambert-Beer law: $A/L = \alpha C$, where A is the absorbance determined at a given wavelength, L is the optical path length, α is the extinction coefficient of the dispersed material at such a wavelength and C is the dispersion concentration. In the present work, the absorbance was measured at a wavelength of 660 nm because it is well within the range (>300 nm) where all the tested solvents are completely transparent and also because it is frequently the wavelength of choice in the literature for quantitative studies of the dispersion behavior of many 2D materials (e.g., graphene).[46] α was estimated on the basis of g-C_3N_4 dispersions prepared in the following solvents: water, isopropanol, dimethyl sulfoxide, and γ–butyrolactone. Aliquots of the corresponding g–C_3N_4 dispersions were taken and sequentially diluted to obtain a series of dispersions with different concentrations, the absorbance of which was measured. The remaining known volume of the as-prepared dispersions was vacuum-filtered through alumina membrane filters and dried overnight in a vacuum oven at 80 ºC, allowed to cool down in a desiccator and finally weighed to calculate its original concentration. Calibration curves relating measured absorbance and g–C_3N_4 concentration for the selected solvents could then be plotted, the slopes of which yielded α. A mean value of α (660 nm) = (5.4±0.2) × 10^2 mL mg^{-1} m^{-1} was determined for g–C_3N_4. We note that the value of α was very similar for all the tested solvents.

2.2 Synthesis and catalytic activity of exfoliated g–C_3N_4–Pd NP hybrids

Exfoliated g–C_3N_4–Pd NP hybrids were obtained through the following procedure: 5 mL of 0.34 mM $PdCl_2$ in ethanol was added to 5 mL of an aqueous dispersion of exfoliated g–C_3N_4 (0.2 mg mL^{-1}). The mixture was subsequently allowed to react at 60 ºC for 90 minutes under magnetic stirring. The resultant product was purified by two cycles of sedimentation via centrifugation (20000*g*, 10 min) and re-suspension in milli-Q water. The catalytic performance of the g–C_3N_4–Pd NP hybrids was evaluated on the basis of two model reactions, namely, the reduction of the nitroarenes 4–NP and 4–NA to 4–aminophenol (4–AP) and *p*-phenylenediamine (*p*-PDA), respectively, using $NaBH_4$ as a reducing agent in water at room temperature. To this end, the reaction progress was monitored by following the change in intensity of one of the optical absorption bands characteristic of the substrate. Specifically, we measured absorbance at 400 nm to monitor the reduction of 4–NP to 4–AP, and at 380 nm to follow the reduction of 4-NA to *p*-PDA.[47] An excess of $NaBH_4$ was added to the reaction mixture

($NaBH_4$:nitroarene molar ratio of 600:1) to ensure a constant concentration of the reducing agent during the reaction. In particular, mixed aqueous solutions containing 0.06 mM of nitroarene, 36 mM of $NaBH_4$, and 1.9-5.7 μg mL^{-1} of g–C_3N_4–Pd NP hybrid with a Pd concentration of 2-6 μM was freshly prepared and hand-shaken for a few seconds before measuring its absorbance at the wavelength specified above at 0.25 s time intervals.

2.3 Cell viability/cytotoxicity of exfoliated g-C_3N_4

Murine fibroblasts (L-929 cell line) were chosen to evaluate the biocompatibility of exfoliated g-C_3N_4, as these fibroblasts are highly stable, fast-growing and commonly used in cell culture studies for cytotoxicity assessment. Graphene oxide (obtained from Graphenea) was also assayed for comparison. The fibroblasts were seeded at a density of 5000 cells/well onto 48–well tissue culture plates made of polystyrene that were pre-coated with a thin film of exfoliated g–C_3N_4. The culture medium used was Dulbecco´s modified Eagle´s medium (DMEM) supplemented with 10% fetal bovine serum (FBS), penicillin (100 U mL^{-1}) and streptomycin (100 mg mL^{-1}), and incubation was carried out at 37 ºC in a 7.5% CO_2 atmosphere. This medium was carefully replaced every two days during cell growth. Prior to fibroblast seeding, the culture plates were treated with 500 μL of pure FBS at 37 ºC for 2 h to facilitate the initial adhesion of the cells. Cell viability and proliferation tests were carried out by means of the MTT assay (Sigma-Aldrich), based on the enzymatic reduction of the tetrazolium dye 3-(4,5-dimethylthiazol-2-yl)-2,5-diphenyltetrazolium bromide (MTT) to its insoluble formazan derivative. Assays were conducted 1, 2 and 5 days after seeding of the fibroblasts, performing each experiment in triplicate. To this end, each well from the seeded culture plates was incubated in 500 μL of MTT solution (1 mg mL^{-1}) at 37 ºC and 5% CO_2 atmosphere for 4 h.[48] Then, the MTT solution was removed, 200 μL of dimethyl sulfoxide were added to solubilize the formazan crystals, and finally the absorbance of this reaction product was measured with a BMG FLUOstar Galaxy microplate reader (MTX Lab Systems, Inc.) at 570 nm and the reference wavelength of 690 nm.

2.4 Characterization techniques

The samples were characterized by UV-vis absorption spectroscopy, inductively coupled plasma-mass spectrometry (ICP–MS), Fourier transform infrared (FTIR) spectroscopy, X-ray photoelectron spectroscopy (XPS), field emission scanning electron microscopy (FE–SEM), transmission electron microscopy (TEM), atomic force microscopy (AFM) and elemental analysis. UV-vis absorption spectra were recorded with a Heλios α spectrophotometer (Thermo Spectronic). ICP–MS analysis was performed with a 7500ce instrument (Agilent) equipped with an octopole collision/reaction cell to destroy interfering ions. FTIR spectroscopy was carried out in transmission mode with a Nicolet 8700 spectrometer (Thermo Scientific), using a KBr pellet with sample concentration of ~1 wt%. The recorded spectrum was the result of coadding 64 interferograms obtained at a resolution of 4 cm^{-1}. XPS measurements were accomplished on a SPECS system at a pressure of 10^{-7} Pa with a non-monochromatic Mg K_α X–ray source operated at 11.81 kV and 100 W. Bulk g–C_3N_4 specimens for XPS analysis were prepared by pressing the powder into pellets by means of a hydraulic press, whereas exfoliated g–C_3N_4 samples were prepared by drop-casting aqueous dispersions onto a metallic sample-holder pre-heated at ~50-60 ºC, which was then allowed to dry. The g–C_3N_4 samples exhibited a charging effect amounting to a binding energy shift of ~2 eV that was corrected a posteriori, using the carbon impurity (adventitious carbon) as a reference. FE-SEM images were acquired on a Quanta FEG

650 system (FEI Company) operated at 30 kV, whereas TEM imaging was performed with a JEOL 2000 EX-II instrument operated at 160 kV. Specimens for TEM were prepared by mixing the sample suspension with an equal volume of ethanol and drop-casting ~40 μL of the resulting mixture onto a copper grid (200 square mesh) covered with a carbon film (Electron Microscopy Sciences), which was then allowed to dry. AFM imaging was performed under ambient conditions with a Nanoscope IIIa Multimode apparatus (Veeco Instruments) in the tapping mode of operation. Rectangular silicon cantilevers with nominal spring constant and resonance frequency of about 40 N m^{-1} and 250-300 kHz, respectively, were employed. Samples for AFM were prepared by drop-casting a small volume (~20-40 μL) of diluted g–C_3N_4 dispersion (~0.02-0.05 mg mL^{-1}) onto either freshly cleaved highly oriented pyrolytic graphite (HOPG) or mica substrates, and allowing it to dry at room temperature. The elemental composition of the starting g–C_3N_4 powder was determined in a LECO CHN-2000 elemental analyzer.

3 Results and discussion

3.1 General characterization of bulk and exfoliated g-C_3N_4

Ideally, g-C_3N_4 should consist of stacked sheets made up exclusively of carbon and nitrogen atoms connected by strong covalent bonds, forming tris-*s*-triazine units as building blocks that in turn are linked to each other by way of tertiary amines. However, actual synthetic approaches usually yield incomplete condensation of the structure, leading to the presence of primary and secondary amines (see Fig. 1). The latter groups should be relatively abundant, as they are expected to be present not only along the periphery of the individual sheets (a natural consequence of the finite particle size) but also at internal edges within the sheets. Furthermore, because such groups are able to establish hydrogen bonds, interlayer interactions in g-C_3N_4 should incorporate not only weak dispersive (van der Waals) forces, as is typical for many well-studied layered materials (graphite, transition metal dichalcogenides, etc), but also a significant hydrogen bonding component. As will be discussed below in the light of the obtained results, this feature should make the colloidal dispersion behavior of exfoliated g–C_3N_4 quite different to that commonly observed for other 2D materials, such as graphene, hexagonal boron nitride or MoS_2, where interlayer interactions are dominated altogether by van der Waals forces.

The starting, bulk g–C_3N_4 material was characterized by means of FE–SEM, elemental analysis, FTIR spectroscopy and XPS. As demonstrated by FE–SEM imaging (Fig. 2a), the g–C_3N_4 powder investigated here consisted of a collection of particles with layered morphology (see inset to Fig. 2a) and significant polydispersity in lateral size (from a few to a few tens of micrometers), a characteristic that has been sometimes attributed to uneven temperature distributions during the synthesis of this compound.[49] According to the results of elemental analysis, the material comprised 34.5 wt. % C and 63.3 wt. % N, yielding a C/N atomic ratio of ~0.64 compared with a value of 0.75 for ideal, fully condensed g–C_3N_4, as well as 1.7 wt. % H, which confirmed its incomplete condensation. Such a considerable amount of H (equivalent to ~19 at. %) is generally reported in the literature for g–C_3N_4 materials[7] and suggests the above-mentioned primary and secondary amine groups to be present in significant numbers. The coexistence of the expected nitrogen-containing heterocycles and uncondensed amine groups in the starting material was substantiated by FTIR spectroscopy (Fig. 2b). Specifically, doubly degenerated bands characteristic of *s*–triazine ring vibrations

appeared at 1573 and 1542 cm^{-1} (quadrant stretching) as well as at 1460 and 1405 cm^{-1} (double semicircle stretching), together with a band at ~809 cm^{-1} (out-of-plane ring bending by sextants).[50] Furthermore, primary amines were detected by the appearance of bands at 3246 cm^{-1} (asymmetric N-H stretching) and 3180 cm^{-1} (symmetric stretching), as well as a strong NH_2 scissoring deformation band at 1639 cm^{-1}.[50]

XPS analysis indicated that only C and N were present in the starting material (survey spectrum not shown), with the exception of some O impurity (<2 at. %) that was also detected (H is not detectable by this technique). Fig. 2c and d show the high resolution C1s and N1s core level spectra, respectively, for the starting, bulk g–C_3N_4 powder. The C1s spectrum was peak-fitted into three components: the main one was located at about 288.2 eV (red trace in Fig. 2c) and attributed to sp^2 C from the *s*-triazine heterocycle, whereas the wide component at 294.0 eV (orange trace) could be ascribed to its $\pi \rightarrow \pi^*$ satellite band;[7] the weak component at ~285 eV (green trace) was associated to carbon impurities. Peak-fitting of the N1s band yielded four components. The main component (~398.6 eV, blue trace in Fig. 2d) corresponded to sp^2 N from the heterocycle,[7] and was also accompanied by a weak, wide $\pi \rightarrow \pi^*$ satellite band at 404.5 eV (cyan trace). Although this weak component has been frequently assigned to charging effects, it is clear that there must be a $\pi \rightarrow \pi^*$ satellite for the N1s signal from the *s*-triazine heterocycle, very much like there is a satellite component for its C1s signal. We also note that the energy difference between the main C1s or N1s component and the corresponding $\pi \rightarrow \pi^*$ satellite is essentially identical for both elements (5.8-5.9 eV), consistent with the idea that it corresponds to the same electronic transition. The component at 400.1 eV (pink trace in Fig. 2d) can be ascribed to tertiary N both from the bridges that connect neighboring tris-*s*-triazine units and from the centre of the tris-*s*-triazine unit itself (see Fig. 1).[7] Finally, the component at 401.2 eV (grey trace) is thought to signal the presence of quaternary nitrogen in the form of positively charged amine functions,[7] as neutral amines would be expected at ~399.5 eV.[51] We interpret that this positively charged nitrogen results from electron ionization of the sample during the XPS experiment.[51] Put together as a whole, the general characterization of bulk g–C3N4 powder points to a significant degree of chemical heterogeneity for this material. Indeed, although there are areas consisting of the ideal fully condensed, nitrogen-containing heterocycles, there are also uncondensed areas, as indicated by the considerable amount of primary and secondary amine groups. This heterogeneity could introduce complexity in the dispersion behavior of this material.

Bath sonication of the bulk g–C_3N_4 powder in a range of solvents (see Supporting Information for the complete list of solvents employed) at a given initial concentration (e.g., 3 mg mL^{-1}), followed by mild centrifugation of the resulting dispersions, afforded in many cases yellowish white supernatants that were indicative of the successful exfoliation and colloidal stabilization of the g–C_3N_4 particles (e.g., see inset to Fig. 3a for a suspension in dimethyl sulfoxide). As exemplified in Fig. 3a, and in agreement with previous reports for g–C_3N_4,[52] UV-vis absorption spectroscopy of such dispersions revealed a strong band at ~320 nm together with a strong shoulder at about 230 nm and a weak one at ~390 nm. Note that in some solvents, especially those with C=C bonds in their structure, the absorption features from the dispersed material could not be properly measured at wavelengths below ~300 nm due to very strong absorbance from the solvent molecules themselves. We assign the shoulder at 230 nm to $\pi \rightarrow \pi^*$ transitions from C=N structures in the tris-*s*-triazine unit, and the main absorption band at 320 nm to $n \rightarrow \pi^*$ transitions from nitrogen lone pairs, either belonging to the extended tris-*s*-triazine structure or to the amine groups at the edges. Although the opposite band assignment has been occasionally proposed in the literature[49,52,53] we believe the one

given here to be correct for the following reasons: (i) absorption bands at ~220 and 270 nm have been previously observed for *s*-triazine and assigned to $\pi \rightarrow \pi^*$ and $n \rightarrow \pi^*$ transitions, respectively,[54] (ii) theoretical calculations have predicted that the top of the valence band in g–C_3N_4 mainly consists of 2p orbitals from N atoms, while hybridized N 2p and C 2p orbitals predominately contribute to the bottom of the conduction band,[55] thereby suggesting that $n \rightarrow \pi^*$ transitions will be the lowest (highest) in energy (wavelength); (iii) as discussed above, XPS suggests that the $\pi \rightarrow \pi^*$ transition in g-C_3N_4 is associated to an energy of 5.8-5.9 eV, or equivalently, to a wavelength of ~210 nm.

Both TEM (Fig. 3b) and AFM (Fig. 3c) imaging provided evidence that the g–C_3N_4 material suspended in the solvents had been exfoliated into thin platelets. The platelets exhibited lateral sizes between ~50 nm and ~1 μm, but mostly in the 100-500 nm range (see upper histogram in Fig. 3d), and were typically a few to several nanometers thick (see overlaid line profile in Fig. 3c, and lower histogram in Fig. 3d), implying that they were of a multi-layered nature. Such morphological features of the exfoliated platelets were seen to be similar for suspensions in different solvents (e.g., isopropanol, *N*,*N*–dimethylformamide or water) and pointed to a relatively limited degree of exfoliation of the g–C_3N_4 powder. This outcome could have probably been anticipated on the basis of the aforementioned observation that interlayer interactions in g–C_3N_4 comprise not only weak van der Waals forces but also comparatively strong hydrogen bonds. The latter should make the cleavage of the g–C_3N_4 layers energetically more demanding than that of other layered solids having just van der Waals cohesive forces. In any event, we note that the exfoliated platelets retained the structural and chemical characteristics of their parent g–C_3N_4 powder. For instance, the high resolution C1s and N1s XPS spectra of the exfoliated platelets processed into thin films (Fig. 3e and f, respectively) were essentially identical to those of their starting, non-exfoliated counterpart (Fig. 2c and d). This result indicates that sonication and interaction with the solvent molecules does not alter the basic make-up of g–C_3N_4 to any significant extent.

3.2 Quantitative analysis of the dispersion behavior of exfoliated g-C_3N_4 in solvents

When a solute is mixed with a solvent, its solubility can be quantitatively analyzed is given by the energetic cost of mixing both components, which in turn can be evaluated in terms of their enthalpy of mixing.[56] This approximation, which was originally developed for molecular solutes,[56] has been successfully used in recent years to understand and predict the dispersion behavior in solvents of different types of nanostructured materials, including pristine graphene,[57–59] reduced graphene oxide,[60] carbon nanotubes [61, 62] and nanofibers [63] as well as several inorganic graphene analogues.[64] When the solute is a 2D material dispersed in a solvent in the form of thin platelets, as in the present case, the enthalpy of mixing per unit volume of solvent ($\overline{\Delta H}_{mix}$) can be written to a first approximation in terms of the surface energy of both solute and solvent as:[46]

$$\overline{\Delta H}_{mix} = \frac{2}{t}(\delta_{2D} - \delta_{sol})^2 \phi \qquad (1)$$

where t is the nanosheet thickness, $\delta_{2D} = \sqrt{E_{surf}^{2D}}$ ($\delta_{sol} = \sqrt{E_{surf}^{sol}}$) is the square root of the surface energy of the 2D material (solvent), and ϕ is the volume fraction of the 2D material in the solvent. Recently, it has been demonstrated that this analysis is equivalent to the approach based on the cohesive energy density of the components.[65] Specifically, when only total cohesive energy densities are considered, $\overline{\Delta H}_{mix}$ can be written as:[64]

$$\overline{\Delta H}_{mix} = (\delta_{T,2D} - \delta_{T,sol})^2 \phi(1-\phi) \quad (2)$$

where ϕ has the same meaning as in equation (1), and $\delta_{T,2D}$ ($\delta_{T,sol}$) is the Hildebrand solubility parameter of the 2D material (solvent), which is equal to the square root of its total cohesive energy density, i. e., $\delta_{T,2D} = \sqrt{E_{coh}^{2D}}$ ($\delta_{T,sol} = \sqrt{E_{coh}^{sol}}$).

According to eqs. (1) and (2), $\overline{\Delta H}_{mix}$ is minimized when the surface energy and the Hildebrand solubility parameter of the 2D material match with those of the solvent. To see how these predictions compare with the actual dispersion behavior of g–C_3N_4, we prepared suspensions in a number of solvents that cover a wide range of surface energy values by sonicating 3 mg mL^{-1} of g–C_3N_4 in the corresponding solvent for 4 hours and centrifuging the resulting mixtures at 500*g* for 10 min, discarding the sediment and keeping the supernatant as the final dispersion. These processing parameters were chosen for practical reasons, as they allowed obtaining, within a reasonable time, good quality dispersions in the most appropriate solvents that were colloidally stable for weeks, showing little amount of sedimentation to the naked eye. We also investigated the effect of the processing parameters on the final amount of exfoliated material colloidally stabilized in dispersion, as explained below. The amount of g–C_3N_4 retained in the supernatant was estimated by measuring its optical absorbance at 660 nm (see Experimental Section). The surface energy of a solvent equals its surface tension plus an entropy-related term that is approximately constant for all solvents, i.e. ~29 mJ m^{-2} at room temperature,[46, 64,66] and thus it is possible, and in fact it is common practice, to discuss the dispersion of solutes in terms of the more readily available surface tensions of the solvents.

Fig. 4a plots the concentration of g–C_3N_4 suspensions against the surface tension of the tested solvents. It can be noticed from Fig. 4a that the amount of dispersed g–C_3N_4 is maximized for solvents with surface tension close to 48 mJ m^{-2}, good solvents being clustered in the ~35-55 mJ m^{-2} range. The ~20 mJ m^{-2} span for the surface tensions of successful solvents is similar to that previously observed for pristine graphene and other nanostructured materials.[57,63,64] In the case of pristine graphene, the most successful solvents display surface tensions in the 35-45 mJ m^{-2} range, in agreement with the experimental surface energy of the basal plane of graphene (~70–80 mJ m^{-2}).[46] For g-C_3N_4, the values of surface tension of the most successful solvents are shifted to somewhat higher (~5–10 mJ m^{-2}) values compared to the case of graphene, which implies that g–C_3N_4 flakes possess a higher surface energy than that of graphene. Indeed, a recent calculation of the surface energy of g–C_3N_4 yielded a relatively high value of ~115 mJ m^{-2}.[67] Such a discrepancy between theoretically calculated surface energy values of materials and the values derived indirectly from colloidal dispersion studies is not unusual and its origin is not well understood.[64] In the present case, many of the best solvents for g–C_3N_4 lay in the upper end of the surface tension range for commonly available solvents. For example, Fig. 4b shows a digital photograph of a representative selection of the suspensions arranged from left to right in increasing order of solvent surface tension. The most successful solvents were diols, e.g. 1,3-butanediol, ethylene glycol or thiodiglycol, and similar difunctional compounds such as ethanolamine or 3-pyridinemethanol, although solvents such as pyridazine and aniline exhibited a reasonably good performance, most of them having surface tension values between 45 and 55 mJ m^{-2}. Therefore, there is the possibility that g–C_3N_4 could be better dispersed in solvents with higher values of surface tension (e.g., 70, 80 or 90 mJ m^{-2}), but solvents within such a range are very scarce or simply not available. Thus, to gain a more accurate insight into the dispersion behavior of this material, we turned our

attention to an analysis based on Hildebrand and, probably more relevantly, Hansen solubility parameters.

Fig. 5a plots the concentration data for the prepared g–C_3N_4 dispersions as a function of the Hildebrand solubility parameter, δ_T, of the solvents. The most successful solvents were mostly constricted to a narrow range of δ_T values around 28-32 $MPa^{1/2}$, which were higher than the values reported for other 2D materials of varied chemical nature but having interlayer interactions dominated by weak van der Waals forces, such as pristine graphene (δ_T range centered at ~22 $MPa^{1/2}$), and transition metal dichalcogenides (~21-23 $MPa^{1/2}$).[64] This result, together with the one obtained from the analysis of the data based on surface energies, suggests that interlayer interactions in g–C_3N_4 are stronger than those existing in graphite or transition metal dichalcogenides, which in turn would be consistent with the idea discussed above that interlayer hydrogen bonding interactions are in place in g–C_3N_4.

To gain more detailed knowledge on the factors that determine the dispersibility of g–C_3N_4, an analysis based on Hansen solubility parameters was carried out, i. e., the total cohesive energy density on which the Hildebrand parameter is based was broken down into its dispersive, polar and hydrogen-bonding components.[56] Indeed, it is well known that while matching Hildebrand solubility parameters of solvent and solute is usually sufficient to identify good solvents for non–polar solutes, a further criterion is often required for polar solutes: good solvents are those with the three Hansen parameters matching their solute counterparts[57] In this case, the enthalpy of mixing of Eq. (2) can be re-written as:

$$\overline{\Delta H}_{mix} = \left[(\delta_{D,2D} - \delta_{D,sol})^2 + (\delta_{P,2D} - \delta_{P,sol})^2 + (\delta_{H,2D} - \delta_{H,sol})^2\right]\phi(1-\phi) \quad (3)$$

with $\delta_{D,2D}$ ($\delta_{D,sol}$), $\delta_{P,2D}$ ($\delta_{P,sol}$), and $\delta_{H,2D}$ ($\delta_{H,sol}$) being respectively the dispersive, polar and hydrogen-bonding Hansen solubility parameters of the 2D material (solvent). A given Hansen solubility parameter equals the square root of the corresponding component of the cohesive energy density. According to Eq. (3), the dispersibility of g–C_3N_4 will be most favored in those solvents that have the three Hansen solubility parameters matching those of the g–C_3N_4 flakes, and therefore the dispersed amount should be expected to peak for a narrow range of values of these three parameters. To identify the optimum Hansen parameters for dispersing g–C_3N_4, we plot in Fig. 5b, c, and d the concentration of the suspensions versus δ_D, δ_P and δ_H, respectively. As can be seen, the dispersed amount was maximized roughly for values of δ_D, δ_P and δ_H, around 17–19, 9–15 and 10–20 $MPa^{1/2}$, respectively. As we have demonstrated in a previous study on the dispersibility of reduced graphene oxide (RGO) in solvents, chemical heterogeneity, leads to a larger scattering in the experimental dispersion data than what is found for more homogeneous materials such as graphene, dichalcogenides, etc.[60] However, though smaller than in the case of RGO, there is also a significant scattering in the data even in the case of such homogeneous materials, suggesting that the Hansen parameters theory does not capture all the complexity of their dispersion behavior. An estimate of the Hansen parameters for g–C_3N_4, obtained from the weighted average of the solubility parameters of the solvents using the concentration value for each dispersion as the weighting factor, yielded the following: $<\delta_{D,g\text{-}C3N4}> \approx 17.8 \pm 0.1$ $MPa^{1/2}$, $<\delta_{P,g\text{-}C3N4}> \approx 10.8 \pm 0.1$ $MPa^{1/2}$ and $<\delta_{H,g\text{-}C3N4}> \approx 15.4 \pm 0.2$ $MPa^{1/2}$. Compared with pristine graphene ($<\delta_D> \approx 18.0$ $MPa^{1/2}$, $<\delta_P> \approx 9.3$ $MPa^{1/2}$ and $<\delta_H> \approx 7.7$ $MPa^{1/2}$)[57] and transition metal dichalcogenides ($<\delta_D> \approx 18$ $MPa^{1/2}$, $<\delta_P> \approx$ 8-9 $MPa^{1/2}$ and $<\delta_H> \approx$ 8-9 $MPa^{1/2}$),[64] the most significant difference was found in the hydrogen-bonding parameter, which was much larger for g–C_3N_4. In line with what has been discussed previously, this result is not unexpected from the chemical structure of non ideal g–C_3N_4 (see Fig.

1): with external and internal edges saturated by primary or secondary amines, g–C_3N_4 layers should be particularly prone to hydrogen bonding and other types of interaction (e.g., acid–base) described by the δ_H parameter. It should thus come to no surprise that most of the successful solvents for g–C_3N_4 contained alcohol or amine groups, which are well known to form hydrogen bonds. In fact, the hydrogen-bonding parameter for g–C_3N_4 was similar to that found previously for other nanostructured materials where hydrogen–bonding played an important role in dispersion due to their high content of oxygen–containing functional groups (hydroxyls, carboxyls, etc), such as reduced graphene oxide ($<\delta_H>\approx$ 14.1 $MPa^{1/2}$)[60] and platelet-type graphite nanofibers ($<\delta_H>\approx$ 14.7 $MPa^{1/2}$).[63] For molecular solutes, the greater strength of hydrogen bonds involving O–H structures against those involving N–H, invariably leads to higher hydrogen–bonding parameters for pairs of analogous compounds containing either O–H or N–H, e. g., δ_H values for methanol and methylamine are 22.3 and 17.3 $MPa^{1/2}$; ethanol and ethylamine (19.4 vs. 10.7 $MPa^{1/2}$); phenol and aniline (14.9 vs. 10.2 $MPa^{1/2}$).[56] The fact that δ_H was slightly higher for g–C_3N_4 compared with the two mentioned oxygen-containing carbon nanostructures suggests that the former material is relatively densely decorated with primary and/or secondary amine groups, which in turn would be consistent with the high hydrogen content of the bulk starting material as determined by elemental analysis.

The three Hansen solubility parameters define a parameter space (the so–called Hansen parameter space), where the shorter the distance between a given solvent and a solute, the better the ability of the solvent to solubilize the solute. Such a distance, *R*, has been defined by Hansen as:[56]

$$R = \sqrt{4(\delta_{D,2D} - \delta_{D,sol})^2 + (\delta_{P,2D} - \delta_{P,sol})^2 + (\delta_{H,2D} - \delta_{H,sol})^2}\,, \quad (4)$$

with the different parameters having the same meaning as in Eq. (3). Fig. 6 depicts the dispersed concentration of g–C_3N_4 against distance between the specific solvent and g–C_3N_4 in the Hansen space, *R*, calculated using the Hansen parameters obtained above for g–C_3N_4. Ideally, the data for all solvents should lie on a line with negative slope, the dispersed amount of g–C_3N_4 increasing with decreasing *R*, but what is usually found, as in the present case, is a rough trend.[60] Such well-documented deviation from the expected behavior can be ascribed to the fact that the Hansen parameter theory does not capture all the details of the solvent-material interaction.

As mentioned above, the effect of different processing parameters, namely, the initial bulk g–C_3N_4 concentration (C_i), sonication time (t_{sonic}), as well as centrifugation speed (ω_{CF}) and time (t_{CF}), on the final amount of exfoliated material colloidally stabilized in dispersion was investigated. Specifically, dispersions of g–C_3N_4 in water, which was identified as a reasonably effective solvent, were prepared keeping three of these parameters constant and setting the remaining one as a variable. The concentration of the resulting dispersions was monitored and is shown in Fig. 7. Initially, the effect of the centrifugation parameters (ω_{CF} and t_{CF}) on g–C_3N_4 concentration (C_i=3 mg mL^{-1}, t_{sonic}=4 h) was assessed. As expected, the concentration decreased with increasing centrifugation rates up to 2000*g* (see Fig. 7a). However, the quality of the dispersion was already good for lower ω_{CF}, e.g., 500g. Indeed, the broad background due to scattering of light that tended to appear in the UV-vis spectra if large, colloidally unstable particles were present was not observed (see Fig. 3a, with C_i=3 mg mL^{-1}, t_{sonic}=4 h, ω_{CF}=500*g* and t_{CF}=10 min), i. e., the protocol used in the current work for preparing g–C_3N_4 dispersions for the dispersibility studies is efficient in removing unexfoliated flakes. Fig. 7b shows the results when working with t_{CF} as a variable. As

could be anticipated, the concentration dropped with increasing t_{CF} until a plateau was reached (at 40 min in this case) where very long-term colloidal stability for these conditions (C_i=3 mg mL^{-1}, t_{sonic}=4 h, ω_{CF}=500*g*) could be attained (months). However, at a shorter t_{CF} of 10 min, the dispersions were already stable for one week, which was enough for our dispersion studies and could suffice in many other cases. Furthermore, for solvents with good performance such as 1-butanol, 1,3-butanediol, and γ-butyrolactone, 40–60 wt. % exfoliated g-C_3N_4 were still dispersed in the solvent after standing for four months, while poorer solvents such as acetic acid retained around 25 wt. % after the same period. As for the effect of initial bulk g–C_3N_4 concentration, C_i, the amount of exfoliated material colloidally stabilized in dispersion increased almost linearly and steeply with C_i up to ~ 10 mg mL^{-1} (for g–C_3N_4 dispersions prepared at t_{sonic}=4 h, ω_{CF}=500*g* and t_{CF}=10 min, see Fig 7c), while the effect was much weaker for higher values of C_i. Indeed, while increasing C_i from 1 to 10 mg mL^{-1} led to a 10-fold increment in the concentration of exfoliated material, doubling C_i from 10 to 20 mg mL^{-1}, led to a marginal increase (< 20 %) in dispersed concentration. This type of behavior has been previously observed in the liquid-phase exfoliation and dispersion via sonication of other 2D materials,[47,68] but its origin remains to be elucidated. As a tentative explanation, it can be argued that the ultrasonic treatment generates a certain density of cavitation bubbles in the medium, the collapse of which is known to trigger the exfoliation of small fragments from the surface of layered materials.[69] It is therefore reasonable to assume that such a density of cavitation bubbles can only cope with the detachment of fragments from a limited number of particles of the layered material simultaneously. As a result, increasing the concentration of particles above a certain level cannot be expected to lead to an equivalent increase in the concentration of exfoliated material dispersed in the solvent. Finally, the effect of t_{sonic} was also assessed (Fig. 7d). It was noticed that the dispersed concentration increased sublinearly with t_{sonic}, similarly to what has been previously observed for a number of systems[70] as a result of the decrease in platelet lateral size induced by sonication.

We note that the dispersed g–C_3N_4 concentrations shown in the ordinate axis for the plots of Figs.4–7 have been determined though measurement of UV–vis absorbance of the corresponding dispersions and using the Lambert-Beer law $A/L = \alpha C$, where A/L is the absorbance per unit optical path length, C is the concentration and α is the extinction coefficient. A/L values measured in all the tested solvents are given in Table S1 of the Supporting Information, together with solvent surface tension and solubility parameters taken from the literature.[56,71] α was determined on the basis of calibration curves obtained as described in the Experimental section. Calibration curves were derived for four different solvents (Fig. 8): water, isopropanol, dimethyl sulfoxide and γ–butyrolactone. As can be seen, the slopes of the four calibrations are very similar. From them, a mean value of (5.4 ± 0.2)×10^2 mL m^{-1} mg^{-1} was obtained for α, which was assumed to be valid for every solvent. With this value, we were also able to determine the maximum g–C_3N_4 concentrations attained with the processing parameters chosen in the study (C_i=3 mg mL^{-1}, t_{sonic}=4 h, ω_{CF}=500g and t_{CF}=10 min), which were around 1 mg mL^{-1} using the best solvents (i. e., ethanolamine, 3-pyridinemethanol or 1,3–butanediol).

3.3 Synthesis and catalytic activity of exfoliated g–C_3N_4–Pd NP hybrids

The preparation of 2D materials in colloidal dispersion enables their further processing or modification through wet techniques, e. g., to prepare composites with polymers or hybrids with metal NPs. As we demonstrated above, the exfoliated g–C_3N_4 flakes retain the chemical structure of their parent bulk material, but possess a higher specific surface

area. This provides a large number of exposed nitrogen-containing groups on the g–C_3N_4 flakes (see Fig. 1) that are expected to act as anchoring sites for the nucleation and growth of metal NPs with the resulting g–C_3N_4–Pd NP hybrids having a high potential in catalytic applications.[72] Indeed, there is a very recent report on the effective decoration of g–C_3N_4 nanosheets with Ag NPs.[73] Herein, we were able to grow Pd NPs selectively on the exfoliated g–C_3N_4 flakes by reduction of a precursor metal salt following a wet chemical method described in the Experimental section. Evidence for decoration of the flakes with the metal NPs was obtained from TEM imaging and XPS. Fig. 9a shows a representative TEM image of the exfoliated g–C_3N_4–Pd NP hybrid. No stand-alone NPs were seen in the images, which implies that the Pd NPs grew exclusively on the g–C_3N_4 flakes. The dispersion of the NPs on the g–C_3N_4 support was good and their density was high. Typical NP sizes were in the range between 3 and 13 nm, with an average size of 6 ± 2 nm. We note that such values are significantly smaller than those reported very recently for Pd NPs supported onto graphene flakes stabilized in water by flavin mononucleotide and prepared with exactly the same methods described here (~10-15 nm),[47] suggesting that the abundant nitrogen surface groups make g–C_3N_4 flakes a better support for metal NPs. The high resolution Pd 3d core level spectrum obtained by XPS for the hybrid (Fig. 9b) confirmed that Pd on the g–C_3N_4 flakes was in metallic form. Indeed, two slightly asymmetrical Pd $3d_{3/2}$ and $3d_{5/2}$ bands centered, respectively, at 340.3 and 335.0 eV, were observed as expected for Pd(0).[74]

The catalytic performance of metal NPs is frequently tested with certain model reactions that involve the reduction of nitroarenes (e. g., 4–NP to 4–AP, and 4–NA to *p*–PDA) with $NaBH_4$ in aqueous medium at room temperature.[75] Such reactions are also useful from a practical point of view as their products are widely used in industry. Specifically, 4-AP is an intermediate for the synthesis of many analgesic and antipyretic drugs (e.g. paracetamol, acetanilide, phentacin, etc)[76] in the pharmaceutical industry, and *p*–PDA is used as hair dye[77] and for the preparation of aramid-based polymers (e.g. Kevlar)[78] Both reactions are thermodynamically favorable but kinetically hindered, and thus require the use of suitable catalysts to proceed at an acceptable rate. Also in both cases, the reaction progress can be followed spectrophotometrically by monitoring the decay of absorption peaks characteristic of the starting nitroarenes. Fig. 10a shows typical UV-vis absorption spectra of aqueous solutions of (i) 4-NP at the slightly acidic pH of deionized water (black plot), (ii) deprotonated 4-NP (i.e., 4-nitrophenoxide ion), formed in the basic medium generated in the presence of $NaBH_4$ (green plot), and (iii) the product of 4-NP reduction, 4-AP (more specifically, its aminophenoxide anion; violet plot). In the reduction of 4-NP, the intensity of the characteristic absorption peak of 4-nitrophenoxide at 400 nm, which does not overlap with those of other species present in the reaction medium, can be taken as a quantitative measure of the reaction progress. Similarly, 4-NA displays a well-defined absorption peak at ~380 nm (Fig. 10c, orange trace) that is not present in its reduced counterpart p-PDA (blue trace), so in this case absorbance at 380 nm can be used to monitor the reaction progress.

No conversion of 4-NP to 4-AP or 4-NA to *p*–PDA (i.e., no decay of the 400 nm or 380 nm peaks, respectively) was observed to occur in the absence of the g–C_3N_4–Pd NPs hybrid or in the presence of only g-C_3N_4 flakes, confirming the catalytic role of the metal NPs. Fig 10b shows a representative experimental kinetic profile obtained for the reduction of 4-NP to 4-AP in the presence of the hybrid. Because $NaBH_4$ was added in large excess compared to the nitroarenes (see Experimental section), it is safe to assume that its concentration remained essentially constant throughout the reaction, and hence the reaction rate can be considered independent of such parameter. Thus, considering

that the time evolution of the absorption peak at 400 nm could be reasonably well fitted to an exponential decay function (Fig. 10b, red line), the reduction reaction can be regarded to obey a pseudo-first-order kinetic behavior with respect to 4-NP, so that the following equation should be applicable:

$$\frac{d[4-NP]}{dt} = -k_{app}[4-NP] \quad (5)$$

, where [4-NP] is the concentration of 4–NP and k_{app} is the apparent reaction rate constant. The measured rate constant for the reduction of 4–NP to 4–AP in the presence of the g–C_3N_4–Pd NPs hybrid was calculated to be k_{app} =(4.3±0.7)×10^{-2} s^{-1}.

The reduction of 4-NA to *p*–PDA was seen to take place much more quickly and displayed a more complex behavior. Indeed, its kinetic profile (Fig. 10d) could not be fitted to a straight line (pseudo–zero–order behavior) or to an exponential decay (pseudo-first-order behavior), being approximately a combination of both. Pseudo-zero order kinetics was in place during the first seconds of the reaction, whereas a predominantly pseudo-first-order behavior set in at later stages. Zero-order kinetic behavior in catalyzed reactions is considered to be originated by the saturation of the catalytically active sites with adsorbed reactant molecules. It is not uncommon to observe, as in the present case, first-order kinetic behavior at the final stretch of a kinetic profile that started showing zero-order kinetic behavior:[79] as the reactants will be nearly consumed at the end of the reaction, it will be less probable for the catalytic sites to be saturated. We believe that the different kinetic behavior between 4–NP and 4–NA reduction has its origin in the presence/absence of electrostatic charge in the substrate involved. First of all, we note that under the basic conditions of the present catalytic reaction (generated by $NaBH_4$), the g–C_3N_4 flakes were found to positively charged in a simple a electrophoretic experiment. Indeed, the flakes were seen to move towards the cathode of a two–electrode system upon application of a bias voltage, while a graphene oxide dispersion, which is known to be negatively charged,[80] moved towards the anode in a similar experiment. Second, as mentioned above, the product of the reduction of 4-NP, i. e., 4–AP is in its negatively charged form (4–aminophenoxide ion) in the reaction medium. Hence, there should be an electrostatic attraction that hinders the desorption of 4–aminophenoxide anions from the vicinity of the g–C_3N_4–Pd NP hybrid. As a result of this electrostatic effect, the reaction progress can be expected to be hindered. On the other hand, 4–NA is expected to be electrically neutral in the $NaBH_4$ medium of the reaction. Consequently, no electrostatic barriers to desorption (or adsorption) of the reaction product (or starting substrate) will be in place in this case, making the saturation of the catalytically active sites of the Pd NPs with adsorbed 4–NA molecules, and hence the observation of zero–order kinetics, a much more likely possibility compared with the case of 4–NP.

To compare the catalytic activity of the g–C_3N_4–Pd NP hybrid with that of other Pd NP-based catalysts reported in the literature for the same reactions, we calculated the turn-over frequency (TOF) of the reaction, defined as the number of moles of substrate (i.e., 4–NP or 4–NA) converted per mole of Pd used in the reaction (determined by ICP–MS) per unit time. Table 1 collects TOF values obtained for our hybrid as well as for a representative set of catalysts based on Pd nanostructures that have been previously studied for the reduction of either 4–NP[81–88] or 4–NA[89–95] with $NaBH_4$. The g–C_3N_4–Pd NP hybrid catalyzed efficiently both reactions. Indeed, its TOF value for the reduction of 4–NP to 4–AP was comparable to that of other good catalysts reported in the literature in recent years, while, to the best of our knowledge, its corresponding value for reduction of 4–NA to *p*–PDA surpassed those hitherto documented for any other Pd-based catalysts. These outstanding activities are thought to arise from a high

catalytically active area, which probably stems from the good dispersion of Pd NPs of relatively small size on the g–C_3N_4 support (see Fig. 9a). Furthermore, unlike the case of unsupported NPs in liquid media, which are usually stabilized by adsorbed surfactants or other dispersants, no capping agents were required here to avoid agglomeration of the g–C_3N_4–Pd NP hybrids. When present, such substances adsorb on the catalytically active sites of the surface, thus hampering access of the substrate molecules to such sites. It is also worth mentioning that the TOF value for 4–NP reduction was substantially lower than that measured for 4–NA reduction. We believe that this could be the result of the electrostatic constraints to desorption of 4–aminophenoxide anions referred to above. Such constraints are not expected to be present in the case of 4–NA, which would explain its faster reaction kinetics.

3.4 Cell growth on exfoliated g-C_3N_4

Finally, 2D materials are generally considered of high potential utility in biomedical applications, and accordingly, significant research efforts in this direction have been devoted over the last years.[96,97] In particular, thin films made up of (or containing) flakes of different 2D materials are promising for, e.g., cell growth and differentiation or tissue regeneration. To this end, it is clear that these films must be highly biocompatible and non cytotoxic. Although previous work has demonstrated that films of 2D materials such as graphene and some transition metal dichalcogenides (e.g., MoS_2 or WS_2) are mostly biocompatible towards a number of human and animal cell lines,[96,97] to the best of our knowledge information on this topic for the case of exfoliated g-C_3N_4 has been generally lacking. Therefore, we have accomplished a preliminary biocompatibility study for thin films of exfoliated g-C_3N_4 towards the murine fibroblast cell line L-929. L-929 is a benchmark cell line commonly used in the evaluation of biocompatibility and cytotoxicity of potential biomedical devices.[98] We deposited thin films of exfoliated g-C_3N_4 from their corresponding aqueous suspensions onto polystyrene culture plates and investigated the proliferation of L-929 cells, seeded on the films at an initial density of 5000 cells per well, on the basis of the MTT assay. For comparison purposes, the experiments were also carried out on thin films of graphene oxide as well as on the bare culture plate.

Fig. 11 presents the results of the proliferation tests 1, 2 and 5 days after cell seeding for culture plates coated with 0.25, 0.5, 0.75 and 1 mg of either exfoliated g-C_3N_4 or graphene oxide, which corresponded to films with estimated thickness values of about 1.5, 3, 4.5 and 6 μm, respectively. In general terms, the murine fibroblasts exhibited good adhesion and proliferation on all the substrates, i.e., on the bare plate as well as on the g-C_3N_4 and graphene oxide films with different thickness. Cell density values were seen to steeply increase with time, implying that the substrates were biocompatible and non cytotoxic. During the first two days, the graphene oxide films tended to perform better than their exfoliated g-C_3N_4 counterparts. This result could be due to the fact that graphene oxide is an extensively oxidized material (typical O/C atomic ratios ~0.4-0.6), and therefore tends to be rather hydrophilic, a feature that is known to promote the initial adhesion of cells on substrates.[99] However, after 5 days the situation was seen to reverse, with g-C_3N_4 displaying either a similar behavior to that of the bare culture plate and graphene oxide (for thinner films) or substantially higher proliferation than that of graphene oxide (for thicker films). Overall, these results suggest that exfoliated g-C_3N_4 is a highly biocompatible 2D material and should warrant the future exploration of its potential in biomedical applications.

4 Conclusions

The dispersion behavior of exfoliated g-C_3N_4 in a wide range of solvents was quantitatively evaluated and the results could be rationalized on the basis of surface energy and Hansen solubility parameters of the tested solvents. Unlike the case of many 2D materials, such as graphene and transition metal dichalcogenides, where interlayer interactions are dominated by weak van der Waals (dispersive) forces, the best solvents for exfoliating and dispersing g-C_3N_4 possessed relatively high values of the hydrogen-bonding parameter (δ_H ~10-25 $MPa^{1/2}$). This result was interpreted to be a consequence of strong hydrogen-bonding interactions between g-C_3N_4 layers that arise from the presence of primary and secondary amine groups in its non ideal, not fully condensed structure. The solvent-exfoliated g-C_3N_4 flakes were also demonstrated to be excellent supports for the synthesis of noble metal (Pd) nanoparticles, and the resulting hybrid materials exhibited an exceptional catalytic activity in the reduction of nitroarenes, in particular 4-nitroaniline. Finally, the results of cell proliferation tests carried out on thin films of exfoliated g-C_3N_4 with murine fibroblasts suggested this 2D material to be biocompatible and non-cytotoxic, thus opening the prospect of its use as substrate for, e.g., tissue engineering or cell growth and differentiation.

Acknowledgments

M. A.–V., S. V.–R.,J. I. P., J. M. M., A. M.–A., and J. M. D. T. gratefully acknowledge financial support from the Spanish MINECO and the European Regional Development Fund (project MAT2011-26399). The same authors also acknowledge partial funding of this work by Plan de Ciencia, Tecnología e Innovación 2013-2017 del Principado de Asturias and European Regional Development Fund through project GRUPIN14-056. A. P., A. A. L-P. and J. L. C. acknowledge financial support from the European Regional Development Fund within the Operative Programme of Región de Murcia 2007-2013. M.A.–V. is thankful for the receipt of a pre-doctoral contract (FPI) from MINECO.

Supporting Information Available: The measured absorbance per unit optical path length of g–C_3N_4 suspensions in all the tested solvents, together with solvent surface tension and Hildebrand/Hansen solubility parameters. This material is available free of charge via the Internet at http: //pubs.acs.org.

References

(1) Novoselov, K. S.; Geim, A. K.; Morozov, S. V.; Jiang, D.; Zhang, Y.; Dubonos, S. V.; Grigorieva, I. V.; Firsov, A. A. Electric Field Effect in Atomically Thin Carbon Films. *Science* **2004**, *306*, 666–669.

(2) Geim, A. K.; Novoselov, K. S. The Rise of Graphene. *Nat. Mater.* **2007**, *6*, 183–191.

(3) Xu, M.; Liang, T.; Shi, M.; Chen, H. Graphene-Like Two-dimensional Materials. *Chem. Rev.* **2013**, *113*, 3766–3798.

(4) Butler, S. Z.; Hollen, S. M.; Cao, L.; Cui, Y.; Gupta, J. A.; Gutiérrez, H. R.; Heinz, T. F.; Hong, S. S.; Huang, J.; Ismach, A. F.; Johnston-Halperin, E.; Kuno, M.; Plashnitsa, V. V.; Robinson, R. D.; Ruoff, R. S.; Salahuddin, S.; Shan, J.; Shi, L.; Spencer, M. G.; Terrones, M.; Windl, W.; Goldberger, J. E. Progress, Challenges, and Opportunities in Two-dimensional Materials beyond Graphene. *ACS Nano* **2013**, *7*, 2898–2926.

(5) Bonaccorso, F.; Lombardo, A.; Hasan, T.; Sun, Z.; Colombo, L.; Ferrrari, A. C. Production and Processing of Graphene and 2D Crystals. *Mater. Today* **2012**, *15*, 564–589.

(6) Nicolosi, V.; Chhowalla, M.; Kanatzidis, M. G.; Strano, M. S.; Coleman, J. N. Liquid Exfoliation of Layered Materials. *Science* **2013**, *340*, 1226419.
(7) Thomas, A.; Fischer, A.; Goettmann, F.; Antonietti, M.; Müller, J.-O.; Schlögl, R.; Carlsson, J. M. Graphitic Carbon Nitride Materials: Variation of Structure and Morphology and their Use as Metal-free Catalysts. *J. Mater. Chem.* **2008**, *18*, 4893–4908.
(8) Gong, Y.; Li, M.; Wang, Y. Carbon Nitride in Energy Conversion and Storage: Recent Advances and Future Prospects. *ChemSusChem* **2015**, *8*, 931–946.
(9) Gong, Y.; Li, M.; Li, H.; Wang, Y. Graphitic Carbon Nitride Polymers: Promising Catalysts or Catalyst Supports for Heterogeneous Oxidation and Hydrogenation. *GreenChem.* **2015**, *17*, 715–736.
(10) Moniz, S. J. A.: Shevlin, S. A.; Martin, D. J.; Guo, Z.-X.; Tang, J. Visible-Light Driven Heterojunction Photocatalysts for Water Splitting – a Critical Review. *Energy Environ. Sci.* **2015**, *8*, 731–759.
(11) Zhu, J.; Xiao, P.; Li, H.; Carabineiro, S. A. C. Graphitic Carbon Nitride: Synthesis, Properties, and Applications in Catalysis. *ACS Appl. Mater. Interfaces* **2014**, *6*, 16449–16465.
(12) Zhao, Z.: Sun, Y.; Dong, F. Graphitic Carbon Nitride Based Nanocomposites: a Review. *Nanoscale* **2015**, *7*, 15–37.
(13) Gong, G.; Zhang, Y.; Pan, Q.; Qiu, J. J. A Fantastic Graphitic Carbon Nitride (g-C_3N_4) Material: Electronic Structure, Photocatalytic and Photoelectronic Properties. *Photochem. Photobiol. C* **2014**, *20*, 33−50.
(14) Cao, S.; Yu, J. g-C_3N_4-Based Photocatalysts for Hydrogen Generation. *J. Phys. Chem. Lett.* **2014**, *5*, 2101–2107.
(15) Goglio, G.; Foy, D.; Demazeau, G. State of Art and Recent Trends in Bulk Carbon Nitrides Synthesis. *Mater. Sci. Eng. R.* **2008**, *58*, 195–227.
(16) Zheng, Y.; Liu, J.; Liang, J.; Jaroniec, M.; Qiao, S. Z. Graphitic Carbon Nitride Materials: Controllable Synthesis and Applications in Fuel Cells and Photocatalysis. *Energy Environ. Sci.* **2012**, *5*, 6717–6731.
(17) Cao, S.; Low, J.; Yu, J.; Jaroniec, M. Polymeric Photocatalysts Based on Graphitic Carbon Nitride. *Adv. Mater.* **2015**, *27*, 2150–2176.
(18) Liu, J.; Zhang, T.; Wang, Z.; Dawson, G.; Chen, W. Simple Pyrolysis of Urea into Graphitic Carbon Nitride with Recyclable Adsorption and Photocatalytic Activity. *J. Mater. Chem.* **2011**, *21*, 14398–14401.
(19) Dong, F.; Wu, L.; Sun, Y.; Fu, M.; Wu, Z.; Lee, S.C. Efficient Synthesis of Polymeric g-C_3N_4 Layered Materials as Novel Efficient Visible Light Driven Photocatalysts. *J. Mater. Chem.* **2011**, *21*, 15171–15174.
(20) Wang, Y.; Wang, X.; Antonietti, M. Polymeric Graphitic Carbon Nitride as a Heterogeneous Organocatalyst: from Photochemistry to Multipurpose Catalysis to Sustainable Chemistry. *Angew. Chem. Int. Ed.* **2012**, *51*, 68–89.
(21) Wang, X. C.; Blechert, S.; Antonietti, M. Polymeric Graphitic Carbon Nitride for Heterogeneous Photocatalysis. *ACS Catal.* **2012**, *2*, 1596–1606.
(22) Chu, S.; Wang, Y.; Guo, Y.; Feng, J.; Wang, C.; Luo, J.; Fan, X.; Zou, Z. G. Band Structure Engineering of Carbon Nitride: In search of a Polymer Photocatalyst with High Photooxidation Property. *ACS Catal.* **2013**, *3*, 912–919.
(23) Liu, G.; Niu, P.; Sun, C.; Smith, S. C; Chen, Z.; Lu, G. Q.; Cheng, H.-M. Unique Electronic Structure Induced High Photoreactivity of Sulfur-doped Graphitic C_3N_4. *J. Am. Chem. Soc.* **2010**, *132*, 11642–11648.

(24) Li, J.; Shen, B.; Hong, Z.; Lin, B.; Gao, B.; Chen, Y. A Facile Approach to Synthesize Novel Oxygen-Doped g-C_3N_4 with Superior Visible-light Photoreactivity. *Chem. Commun.* **2012**, *48*, 12017–12019.
(25) Kim, M.; Hwang, S.; Yu, J.-S. Novel Ordered Nanoporous Graphitic C_3N_4 as a Support for Pt-Ru Anode Catalyst in Direct Methanol Fuel Cell. *J. Mater. Chem.* **2007**, *17*, 1656–1659.
(26) Xu, J.; Shen, K.; Xue, B.; Li, Y.-X.; Cao, Y. Synthesis of Three-Dimensional Mesostructured Graphitic Carbon Nitride Materials and their Application as Heterogeneous Catalysts for Knoevenagel Condensation Reactions. *Catal. Lett.* **2013**, *143*, 600–609.
(27) Xiang, Q.; Yu, J.; Jaroniec, M. Preparation and Enhanced Visible-light Photocatalytic H_2- Production Activity of Graphene/C_3N_4 Composites. *J. Phys. Chem. C* **2011**, *115*, 7355–7363.
(28) Fu, J.; Chang, B.; Tian, Y.; Xi, F.; Dong, X. Novel C_3N_4-CdS Composite Photocatalysts with Organic-Inorganic Heterojunctions: In Situ Synthesis, Exceptional activity, High Stability and Photocatalytic Mechanism. *J. Mater. Chem. A* **2013**, *1*, 3083–3090.
(29) Oh, J.; Lee, S. ; Zhang, K. ; Hwang, J. O.; Han, J.; Park, G.; Kim, S. O.; Park, J. H.; Park, S. Graphene Oxide-Assisted Production of Carbon Nitrides Using a Solution Process and their Photocatalytic Activity. *Carbon* **2014**, *66*, 119–125.
(30) Wei, W.; Jacob, T. Strong Excitonic Effects in the Optical Properties of Graphitic Carbon Nitride g-C_3N_4 from First Principles. *Phys. Rev. B* **2013**, *87*, 085202.
(31) Niu, P.; Zhang, L.; Liu, G.; Cheng, H.-M. Graphene-Like Carbon Nitride Nanosheets for Improved Photocatalytic Activities. *Adv. Funct. Mater.* **2012**, *22*, 4763-4770.
(32) Du, A.; Sanvito, S.; Li, Z.; Wang, D.; Jiao, Y.; Liao, T.; Sun, Q.; Ng, Y. H.; Zhu, Z.; Amal, R.; Smith, S. C. Hybrid Graphene and Graphitic Carbon Nitride Nanocomposite: Gap Opening, Electron-Hole Puddle, Interfacial Charge Transfer, and Enhanced Visible Light Response. *J. Am. Chem. Soc.* **2012**, *134*, 4393–4397.
(33) Cai, M.; Thorpe, D.; Adamson, D. H.; Schniepp, H. C. Methods of Graphite Exfoliation. *J. Mater. Chem.* **2012**, *22*, 24992–25002.
(34) Sham, A. Y. W.; Notley, S. M. A Review of Fundamental Properties and Applications of Polymer–Graphene Hybrid Materials. *Soft Matter* **2013**, *9*, 6645–6653.
(35) Quinn, M: D. J.; Ho, N. H.; Notley, S. M. Aqueous Dispersions of Exfoliated Molybdenum Disulfide for Use in Visible-light Photocatalysis. *ACS Appl. Mater. Interfaces* **2013**, *5*, 12751−12756.
(36) Xu, J.; Zhang, L.; Shi, R.; Zhu, Y. Chemical Exfoliation of Graphitic Carbon Nitride for Efficient Heterogeneous Photocatalysis. *J. Mater. Chem.* A **2013**, *1*, 14766–14772.
(37) Yang, S.; Gong, Y.; Zhang, J.; Zhan, L.; Ma, L.; Fang, Z.; Vajtai, R.; Wang, X.; Ajayan, P. M. Exfoliated Graphitic Carbon Nitride Nanosheets as Efficient Catalysts for Hydrogen Evolution under Visible Light *Adv. Mater.* **2013**, *25*, 2452–2456.
(38) Chen, L.; Huang, D.; Ren, S.; Dong, T.; Chi, Y.; Chen, G. Preparation of Graphite-Like Carbon Nitride Nanoflake Film with Strong Fluorescent and Electrochemiluminescent Activity. *Nanoscale* **2013**, *5*, 225–230.
(39) Zhao, H.; Yu, H.; Quan, X.; Chen, S.; Zhang, Y.; Zhao, H.; Wang, H. Fabrication of Atomic Single Layer Graphitic-C_3N_4 and its High Performance of Photocatalytic Disinfection under Visible Light Irradiation. *App. Catal. B: Environ.* **2014**, *152-153*, 46–50.

(40) Wu, S.-Z.; Yu, Y.-X.; Zhang, W.-D. Processing Graphitic Carbon Nitride for Improved Photocatalytic Activity. *Mater. Sci. Semicond. Proc.* **2014**, *24*, 15–20.
(41) Xu, H.; Yan, J.; She, X.; Xu, L.; Xia, J.; Xu, Y.; Song, Y.; Huang, L.; Li, H. Graphene-analogue Carbon Nitride: Novel Exfoliation Synthesis and its Application in Photocatalysis and Photoelectrochemical Selective Detection of Trace Amount of Cu^{2+}. *Nanoscale* **2014**, *6*, 1406–1415
(42) Zhang, X.; Xie, X.; Wang, H.; Zhang, J.; Pan, B.; Xie, Y. Enhanced Photoresponsive Ultrathin Graphitic-phase C_3N_4 Nanosheets for Bioimaging. *J. Am. Chem.. Soc.* **2013**, *135*, 18–21.
(43) Štengl, V.; Henych, J.; Slušná, M.; Ecorchard, P. Ultrasound Exfoliation of Inorganic Analogues of Graphene. *Nanoscale Res. Lett.* **2014**, *9*, 167.
(44) She, X.; Xu, H.; Xu, Y.; Yan, J.; Xia, J.; Xu, L.; Song, Y.; Jiang, Y.; Zhang, Q.; Li, H. Exfoliated Graphene-Like Carbon Nitride in Organic Solvents: Enhanced Photocatalytic Activity and Highly Selective and Sensitive Sensor for the Detection of Trace Amounts of Cu^{2+}. *J. Mater. Chem. A* **2014**, *2*, 2563–2570
(45) Lin, Q.; Li, L.; Liang, S.; Liu, M.; Bi, J.; Wu, L. Efficient Synthesis of Monolayer Carbon Nitride 2D nanosheet with Tunable Concentration and Enhanced Visible-light Photocatalytic Activities. *Appl. Catal. B: Environ.* **2015**, *163*, 135–142.
(46) Hernandez, Y.; Nicolosi, V.; Lotya, M.; Blighe, F.M.; Sun, Z.; De, S.; McGovern, I.T.; Holland, B.; Byrne, M.; Gun'ko, Y.K.; Boland, J.J.; Niraj, P.; Duesberg, G.; Krishnamurthy, S.; Goodhue, R.; Hutchison, J.; Scardaci, V.; Ferrari, A.C.; Coleman, J.N. High-yield Production of Graphene by Liquid-phase Exfoliation of Graphite. *Nat. Nanotechnol.* **2008**, *3*, 563–568.
(47) Ayán-Varela, M.; Paredes, J. I.; Guardia, L.; Villar-Rodil, S.; Munuera, J. M.; Díaz-González, M.; Fernández-Sánchez, C.; Martínez-Alonso, A.; Tascón, J. M. D. Achieving Extremely Concentrated Aqueous Dispersions of Graphene Flakes and Catalytically Efficient Graphene-Metal Nanoparticle Hybrids with Flavin Mononucleotide as a High-performance Stabilizer. *ACS Appl. Mater. Interfaces* **2015**, *7*, 10293–10307.
(48) Vistica, D. T.; Skehan, P.; Scudiero, D:; Monks, A.; Pittman, A.; Boyd, M. R. Tetrazolium-based Assays for Cellular Viability: A Critical Examination of Selected Parameters Affecting Formazan Production. *Cancer Res.* **1991**, *51*, 2515–2520.
(49) Li, X.; Zhang, J.; Shen, L.; Ma, Y:; Lei, W.; Cui, Q.; Zou, G. Preparation and Characterization of Graphitic Carbon Nitride through Pyrolysis of Melamine. *Appl. Phys. A* **2009**, *94*, 389–392.
(50) Lin-Vien, D.; Colthup, N. B.; Fatelley, W. G.; Grasselli, J. G. *The Handbook of Infrared and Raman Characteristic Frequencies of Organic Molecules*, 1st ed; Academic Press Inc.: San Diego, CA, 1991; pp. 160,161, and 300.
(51) Raymundo-Piñero, E.; Cazorla-Amorós, D.; Linares-Solano, A.; Find, J.; Wild, U.; Schlögl, R. Structural Characterization of N-Containing Activated Carbon Fibers Prepared from a Low Softening Point Petroleum Pitch and a Melamine Resin. *Carbon* **2002**, *40*, 597–608.
(52) Li, Q.; He, Y.; Peng, R. Graphitic Carbon Nitride (g-C_3N_4) as a Metal–free Catalyst for Thermal Decomposition of ammonium Perchlorate. *RSC Adv.* **2015**, *5*, 24507–24512.
(53) Guo, Q.; Xie, Y.; Wang, X.; Lv, S.; Hou, T.; Liu, X. Characterization of Well-Crystallized Graphitic Carbon Nitride Nanocrystallites via a Benzene-thermal Route at Low Temperatures. *Chem. Phys. Lett.* **2003**, *380*, 84–87.

(54) Quirke, J. M. E. *1,3,5-Triazines in Comprehensive Heterocyclic Chemistry*; Vol. 3, Katritzky, A. R., Ed.; Pergamon Press: Oxford, New York, Toronto, Sydney, Paris, and Frankfurt, 1984; Vol. 3, p. 464.
(55) Wei, W., Jacob, T. Strong Excitonic Effects in the Optical Properties of Graphitic Carbon Nitride g-C_3N_4 from First Principles. *Phys. Rev. B* **2013**, *87*, 085202.
(56) Hansen, C. M. *Hansen Solubility Parameters: A User's Handbook*, 1st ed; CRC Press: Boca Raton: 2007.
(57) Hernandez, Y; Lotya, M; Rickard, D; Bergin, S. D; Coleman, J. N. Measurement of Multicomponent Solubility Parameters for Graphene Facilitates Solvent Discovery. *Langmuir* **2010**, *26*, 3208–3213.
(58) Yi, M.; Shen, Z.; Ma, S.; Zhang, X. A Mixed-Solvent Strategy for Facile and Green Preparation of Graphene by Liquid-Phase Exfoliation of Graphite. *J Nanopart Res* **2012**, *14*,1003.
(59) Yi, M.; Shen, Z.; Zhang, X.; Ma, S. Achieving Concentrated Graphene Dispersions in Water/Acetone Mixtures by the Strategy of Tailoring Hansen Solubility Parameters. *J Phys D: Appl Phys* **2013**, *46*, 025301.
(60) Ayán-Varela, M.; Paredes, J. I.; Villar-Rodil, S.; Rozada, R.; Martínez-Alonso, A.; Tascón, J. M. D. A Quantitative Analysis of the Dispersion Behavior of Reduced Graphene Oxide in Solvents. *Carbon* **2014**, *75*, 390–400.
(61) Detriche, S.; Zorzini, G.; Colomer, J. F.; Fonseca, A.; Nagy, J. B. Application of the Hansen Solubility Parameters Theory to Carbon Nanotubes. *J Nanosci Nanotechnol* **2008**, *8*, 6082–6092.
(62) Bergin, S. D.; Sun, Z.; Rickard, D.; Streich, P. V.; Hamilton, J. P.; Coleman, J. N. Multicomponent Solubility Parameters for Single-walled Carbon Nanotube-solvent Mixtures. *ACS Nano* **2009**, *3*, 2340–2350.
(63) Guardia, L.; Paredes J. I.; Villar-Rodil, S.; Rouzaud, J.-N.; Martínez-Alonso, A.; Tascón, J. M. D. Discovery of Effective Solvents for Platelet-type Graphite Nanofibers. *Carbon* **2013**, *53*, 222–230.
(64) Cunningham, G.; Lotya, M.; Cucinotta, C. S.; Sanvito, S.; Bergin, S. D.; Menzel, R.; Shaffer, M. S. P; Coleman, J. N. Solvent Exfoliation of Transition Metal Dichalcogenides: Dispersibility of Exfoliated Nanosheets Varies only Weakly between Compounds. *ACS Nano* **2012**, *6*, 3468–3480.
(65) Hughes, J. M.; Aherne, D.; Coleman, J. N. Generalizing Solubility Parameter Theory to Apply to One- and Two-dimensional Solutes and to Incorporate Dipolar Interactions. *J Appl. Polym. Sci.* **2013**,130, 4483–4491.
(66) H.-J. Butt, K. Graf, M. Kappl. *Physics and Chemistry of Interfaces*; Wiley-VCH: Weinheim, 2003, p. 36.
(67) Zhang, X.; Xie, X.; Wang, H.; Zhang, J.; Pan, B.; Xie, Y. Enhanced Photoresponsive Ultrathin Graphitic-phase C_3N_4 Nanosheets for Bioimaging. *J. Am. Chem. Soc.* **2013**, *135*, 18−21.
(68) Guardia, L.; Paredes, J. I.; Rozada, R.; Villar-Rodil, S.; Martínez-Alonso, A.; Tascón, J. M. D.. Production of Aqueous Dispersions of Inorganic Graphene Analogues by Exfoliation and Stabilization with non-Ionic Surfactants. *RSC Adv.* **2014**, *4*, 14115–14127.
(69) Bang, J. H.; Suslick, K. S. Applications of Ultrasound to the Synthesis of Nanostructured Materials. *Adv. Mater.* **2010**, *22*, 1039–1059.
(70) Hanlon, D.; Backes, C.; Higgins, T. M.; Hughes, M.; O'Neill, A.; King, P.; McEvoy, N.; Duesberg, G. S.; Mendoza Sanchez, B.; Pettersson, H.; Nicolosi, V.; Coleman, J. N. Production of Molybdenum Trioxide Nanosheets by Liquid Exfoliation

and Their Application in High-performance Supercapacitors. *Chem. Mater*. **2014**, *26*, 1751−1763.
(71) Lide, D. R. *CRC Handbook of Chemistry and Physics*. CRC Press; 86th ed: Boca Raton, 2005,
(72) Bhowmik, T.; Kundu, M. K.; Barman, S. Ultra Small Gold Nanoparticles–Graphitic Carbon Nitride Composite: an Efficient Catalyst for Ultrafast Reduction of 4-Nitrophenol and Removal of Organic Dyes from Water. *RSC Adv.* **2015**, *5*, 38760–38773.
(73) Bing, W.; Chen, Z.; Sun, H.; Shi, P.; Gao, N.; Ren, J.; Qu, X. Visible-light-driven Enhanced Antibacterial and Biofilm Elimination Activity of Graphitic Carbon Nitride by Embedded Ag Nanoparticles. *Nano Res.* **2015**, *8*, 1648–1658.
(74) B. V. Crist, *Handbook of Monochromatic XPS Spectra. The Elements & Native Oxides*; XPS International LLC: California, USA, 2004, vol. 1, pp. 204–207.
(75) T. Aditya, A. Pal, T. Pal. Nitroarene Reduction: a Trusted Model Reaction to Test Nanoparticle Catalysts. *Chem. Commun.* **2015**, *51*, 9410–9431.
(76) Rode, C.V.; Vaidya, M.J.; Chaudhari, R.V. Synthesis of p-Aminophenol by Catalytic Hydrogenation of Nitrobenzene. *Org. Process Res. Dev.* **1999**, *3*, 465–470.
(77) Wang, S.-P.; Huang, T.-H.. Separation and Determination of Aminophenols and Phenylenediamines by Liquid Chromatography and Micellar Electrokinetic Capillary Chromatography. *Anal. Chim. Act.* **2005**, *534*, 207–214.
(78) Tanner, D.; Fitzgerald, J. A.; Phillips. B. R. The Kevlar Story – an Advanced Materials Case Study. *Angew. Chem. Int. Ed.*. **1989**, *28*, 649–654.
(79) N. K. Pandit. *Introduction to the Pharmaceutical Sciences*, 1st ed; Lippincott Williams & Wilkins: Baltimore (USA), 2007, p.59.
(80) Li, D.; Müller, M. B.; Gilje, S.; Kaner, R. B.; Wallace, G. G. Processable Aqueous Dispersions of Graphene Nanosheets. *Nat. Nanotechnol.* **2008**, *3*, 101–105.
(81) Halder, A.; Patra, S.; Viswanath, B.; Munichandraiah, N.; Ravishankar, N.. Porous, Catalytically Active Palladium Nanostructures by Tuning Nanoparticle Interactions in an Organic Medium. *Nanoscale*, **2011**, *3*, 725–730.
(82) Xue, Y.; Lu, X.; Bian, X.; Lei, J.; Wang, C. Facile Synthesis of Highly Dispersed Palladium/Polypyrrole Nanocapsules for Catalytic Reduction of p-Nitrophenol. *J. Colloid Interface Sci.* **2012**, *379*, 89–93.
(83) Wang, Z.; Xu, C.; Gao, G.; Li, X. Facile Synthesis of Well-Dispersed Pd–Graphene Nanohybrids and their Catalytic Properties in 4-Nitrophenol Reduction. *RSC Adv.* **2014**, *4*, 13644–13651.
(84) Sun, T.; Zhang, Z.; Xiao, J.; Chen, C.; Xiao, F.; Wang, S.; Liu, Y. Facile and Green Synthesis of Palladium Nanoparticles-Graphene-Carbon Nanotube Material with High Catalytic Activity. *Sci. Rep*. **2013**, *3*, 2527(1–6).
(85) Imura, Y.; Tsujimoto, K.; Morita, C.; Kawai, T. Preparation and Catalytic Activity of Pd and Bimetallic Pd−Ni Nanowires. *Langmuir* **2014**, *30*, 5026−5030.
(86) Le, X.; Dong, Z.; Liu, Y.; Jin, Z.; Huy, T.-D.; Le, M.; Ma, J. Palladium Nanoparticles Immobilized on Core–shell Magnetic Fibers as a Highly Efficient and Recyclable Heterogeneous Catalyst for the Reduction of 4-Nitrophenol and Suzuki Coupling Reactions. *J. Mater. Chem. A* **2014**, *2*, 19696–19706.
(87) Zhang, Z.; Xiao, F.; Xi, J.; Sun, T.; Xiao, S.; Wang, H.; Wang, S.; Liu, Y. Encapsulating Pd Nanoparticles in Double-Shelled Graphene@Carbon Hollow Spheres for Excellent Chemical Catalytic Property. *Sci. Rep.* **2014**, *4*, 4053.

(88) Gu, X.; Qi, W.; Xu, X.; Sun, Z.; Zhang, L.; Liu, W.; Pan, X.; Su, D. Covalently Functionalized Carbon Nanotube Supported Pd Nanoparticles for Catalytic Reduction of 4-Nitrophenol. *Nanoscale* **2014**, *6*, 6609–6616.
(89) Karaoglu, E.; Özel, U.; Caner, C.; Baykal, A.; Summak, M. M.; Sözeri, H. Synthesis and Characterization of NiFe 2O 4–Pd Magnetically Recyclable Catalyst for Hydrogenation Reaction. *Mat. Research Bulletin* **2012**, *47*, 4316–4321.
(90) Karaoglu, E.; Baykal, A. $CoFe_2O_4$–Pd (0) Nanocomposite: Magnetically Recyclable Catalyst. *J. Supercond. Nov. Magn.* **2014**, *27*, 2041–2047.
(91) Baykal, A.; Karaoglu, E.; Sözeri, H.; Uysal, E.; Toprak, M. S. Synthesis and Characterization of High Catalytic Activity Magnetic Fe_3O_4 Supported Pd Nanocatalyst. *J. Supercond. Nov. Magn.* **2013**, *26*, 165−171.
(92) Kong, L.; Lu, X.; Jin, E.; Jiang, S.; Bian, X.; Zhang, W.; Wang, C. Constructing Magnetic Polyaniline/Metal Hybrid Nanostructures using Polyaniline/Fe_3O_4 Composite Hollow Spheres as Supports. *J. Solid State Chem.* **2009**, *182*, 2081–2087.
(93) Yang, M.-Q.; Pan, X.; Zhang, N.; Xu, Y.-J. A Facile One-step Way to Anchor Noble Metal (Au, Ag, Pd) Nanoparticles on a Reduced Graphene Oxide Mat with Catalytic Activity for Selective Reduction of Nitroaromatic Compounds. *CrystEngComm* **2013**, *15*, 6819–6828.
(94) Karaoglu, E.; Summak, M. M.; Baykal, A.; Sözeri, H.; Toprak, M.S. Synthesis and Characterization of Catalytically Activity Fe_3O_4-3-Aminopropyltriethoxysilane/Pd Nanocomposite. *J. Inorg. Organomet. Polym.* **2013**, 23, 409−417.
(95) Hsiao, S.-C.; Ou, J.-L.; Huang, M.-S.; Chang, C.-P.; Sung, Y.; Ger, M.-D. Ampholyte Polystyrene Spheres Self-regulated Deposition of Noble Metal Nanoparticles for Catalyst Applications. *Colloid. Polym. Sci.* **2010**, *288*, 1611–1619.
(96) Mao, H. Y. ; Laurent, S. ; Chen, W. ; Akhavan, O. ; Imani, M. ; Ashkarran, A. A. ; Mahmoudi, M. Graphene: Promises, Facts, Opportunities, and Challenges in Nanomedicine. *Chem. Rev.* **2013**, *113*, 3407−3424.
(97) Chen, Y.; Tan, C.; Zhang, H.; Wang, L. Two-dimensional Graphene Analogues for Biomedical Applications. *Chem. Soc. Rev.* **2015**, *44*, 2681–2701.
(98) Biological Evaluation of Medical Devices. Part 5: Tests for in Vitro Cytotoxicity. ISO 10993–5: 2009.
(99) Yan, X.; Chen, J.; Yang, J.; Xue, Q.; Miele, P. Fabrication of Free–standing, Electrochemically Active, and Biocompatible Graphene Oxide−Polyaniline and Graphene−Polyaniline Hybrid Papers. *ACS Appl. Mater. Interfaces* **2010**, *2*, 2521–2529.

Table 1. Comparison of turn-over frequency (TOF) values for different Pd–based catalysts in the reduction of 4–NP and 4–NA with $NaBH_4$.

Catalyst	**TOF (min^{-1})**	**Ref.**
Reduction of 4–NP		
g–C_3N_4–Pd NP hybrid	3.1	Present work
Porous Pd nanoclusters	0.005	81
Pd NPs	0.5	82
Pd-NP/functionalized reduced graphene oxide (rGO)	0.5	83
Pd NPs/rGO/carbon nanotube (CNT)	1.7	84
Amidoamine-templated Pd NPs	1.7	85
Amidoamine-templated Pd nanowires	2.1	85
Pd NPs/Fe_3O_4@fibrous silica nanospheres	3.1	86
Pd NPs in graphene@carbon hollow spheres	4.56	87
Pd NPs on covalently functionalized CNTs	18	88
Reduction of 4–NA		
g-C_3N_4-Pd NP hybrid	36	Present work
Pd NPs	~0.15	89
$NiFe_2O_4$-Pd NP hybrid	3.0	89
$CoFe_2O_4$-Pd NP hybrid	3.0	90
Fe_3O_4-supported Pd NPs	3	91
polyaniline/Fe_3O_4/Pd NP hybrids	0.25	92
commercial Pd/Carbon	0.07	92
Pd NPs/rGO	0.42	93
Fe_3O_4−3-aminopropyl-triethoxysilane/Pd composite	2.0	94
Pd NPs supported onto polystyrene spheres	2.9	95

Figure captions

Figure 1. Chemical structure of tris-*s*-triazine allotrope of g-C_3N_4 indicating the primary amine ($–NH_2$) and secondary amine (>NH) groups present in a non ideal, not fully condensed structure.

Figure 2. General characterization of the starting g-C_3N_4 material: **(a)** representative FE-SEM images; **(b)** FTIR spectrum; (**c**,**d**) high resolution C1s **(c)** and N1s **(d)** core level spectra.

Figure 3. (a) Typical UV-vis absorption spectrum of exfoliated g-C_3N_4 colloidal dispersion. Inset: digital photograph of a dispersion in dimethyl sulfoxide. **(b)** Representative TEM image of exfoliated g-C_3N_4 platelet. **(c)** Typical AFM image of g-C_3N_4 dispersion deposited onto an HOPG substrate, with a superimposed line profile (black trace) taken along the marked white line. **(d)** Histograms of nanosheet lateral size distribution derived from the TEM images (top) and thickness derived from AFM (bottom). **(e,f)** High resolution C1s **(e)** and N1s **(f)** XPS spectra of exfoliated g-C_3N_4 platelets processed into a thin, continuous film.

Figure 4. (a) Exfoliated g–C_3N_4 concentration versus solvent surface tension (γ) at 25 ° C. **(b)** Digital photograph of suspensions of g-C_3N_4 prepared in (from left to right): hexane, isopropanol, acetone, 1-butanol, acetic acid, cyclopentanone, 1,3-butanediol, dimethyl sulfoxide, γ-butyrolactone, etilenglicol, thioglycol, and water. The numbers indicate the surface tension of the corresponding solvent.

Figure 5. Concentration of g–C_3N_4 dispersions as a function of **(a)** the Hildebrand solubility parameter, δ_T, and **(b–d)** the three Hansen parameters, δ_D **(b)**, δ_P **(c)** and δ_H **(d)**, of the solvents at 25 ° C.

Figure 6. Concentration of g–C_3N_4 dispersions against the distance between the specific solvent and g-C_3N_4 in the Hansen space, *R*.

Figure 7. Dispersed g–C_3N_4 concentration as a function of as centrifugation speed (ω_{CF}) **(a)**, centrifugation time (t_{CF}) **(b)**, initial bulk g–C_3N_4 concentration (C_i) **(c)**, and sonication time (t_{sonic}) **(d)**.

Figure 8. Lambert-Beer plot for g–C_3N_4 dispersions prepared in water (blue circles), isopropanol (green squares), dimethyl sulfoxide (red triangles), and γ–butyrolactone (black diamonds). Fittings of the four data sets to straight lines are shown as dotted lines in the same color as the symbols of the corresponding data points.

Figure 9. Characterization of the exfoliated g–C_3N_4–Pd NPs hybrids. **(a)** Representative TEM image. **(b)** High resolution XPS spectrum of Pd 3d core level.

Figure 10. (a) UV–vis absorption spectra of 4-NP (black curve), 4–nitrophenoxide ion (dark yellow), and 4–aminophenoxide ion (violet). The absorption peak at 400 nm of 4-nitrophenoxide is used to monitor its conversion to 4–aminophenoxide by reduction with $NaBH_4$. **(b)** Plot of absorbance at 400 nm for the reduction of 4–nitrophenoxide with $NaBH_4$ in aqueous medium in the presence of g–C_3N_4–Pd NP hybrid. The experimental kinetic profile could be fitted to an exponential decay function, which is

shown as an overlaid red line. The corresponding apparent rate constant (k_{app}) is also shown. Experimental conditions: [4–NP]= 0.06 mM; [$NaBH_4$] = 36 mM; [Pd] = 0.6 μg mL^{-1}. **(c)** UV–vis absorption spectra of 4–NA (orange trace) and *p*-PDA (blue). The absorption peak at 380 nm of 4-NA is used to monitor the reaction progress. **(d)** Plot of absorbance at 380 nm for the reduction of 4–NA with $NaBH_4$ as catalyzed by g–C_3N_4–Pd NP hybrid. Experimental conditions: [4–NA]= 0.06 mM; [$NaBH_4$] = 36 mM; [Pd] = 0.2 μg mL^{-1}.

Figure 11. Results of L-929 cell proliferation tests, based on the MTT assay, for thin films consisting of the amounts indicated of exfoliated g-C_3N_4 (yellow bars), as well as GO (brown bars), deposited from their corresponding aqueous dispersions onto polystyrene culture plates. The cyan bars correspond to tests performed on the bare culture plate. Results of the MTT assay 1 **(a)**, 2 **(b)** and 5 **(c)** days after L-929 cell seeding are shown.

Figure 1

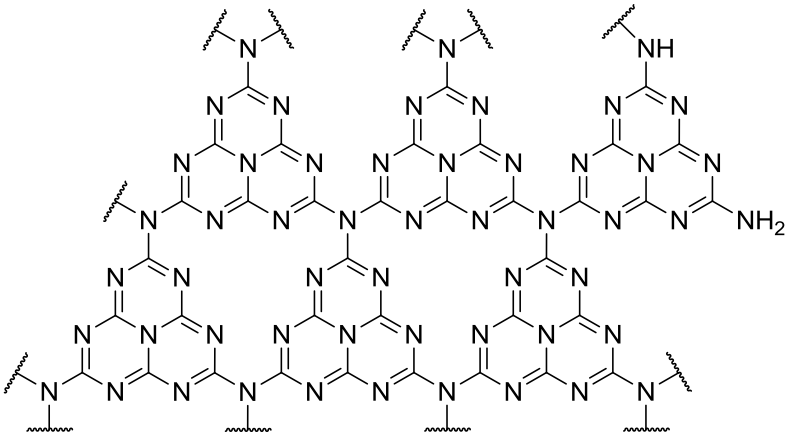

Figure 2

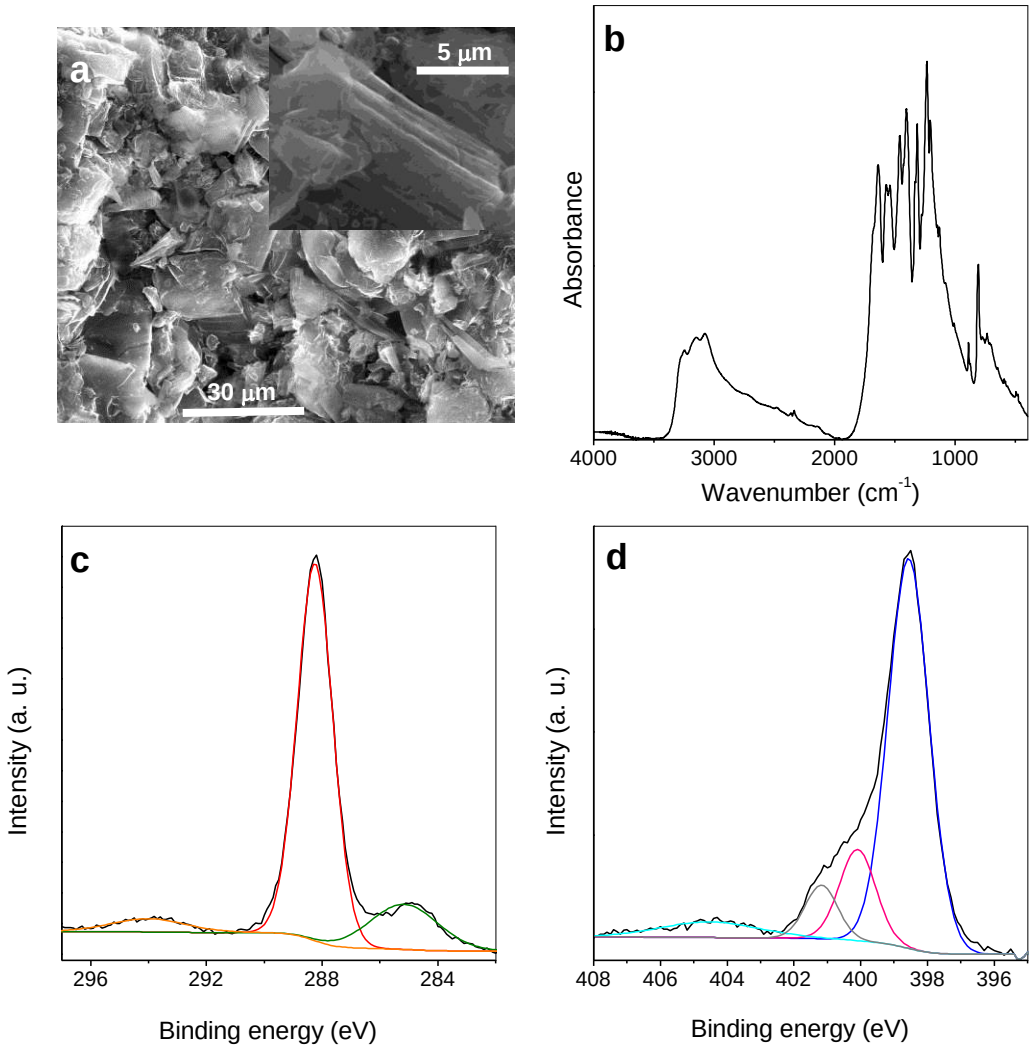
a
5 μm
30 μm
b
Absorbance
4000
3000
2000
1000
Wavenumber (cm-1)
c
Intensity (a. u.)
296
292
288
284
Binding energy (eV)
d
Intensity (a. u.)
408
406
404
402
400
398
396
Binding energy (eV)

Figure 3

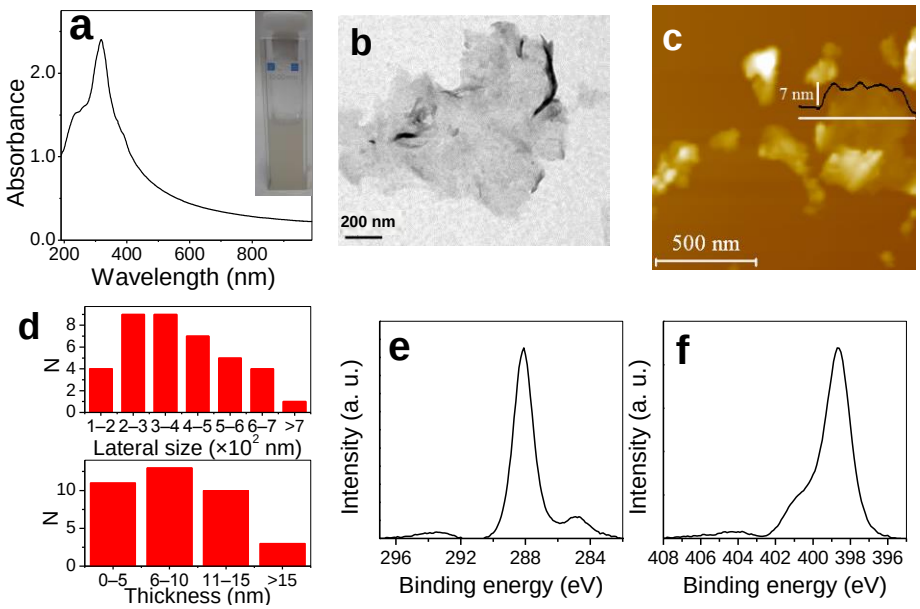
a
Absorbance
2.0
1.0
0.0
200
400
600
800
Wavelength (nm)
b
200 nm
c
7 nm
500 nm
d
N
8
6
4
2
0
1–2 2–3 3–4 4–5 5–6 6–7 >7
Lateral size (×10² nm)
N
10
5
0
0–5 6–10 11–15 >15
Thickness (nm)
e
Intensity (a. u.)
296 292 288 284
Binding energy (eV)
f
Intensity (a. u.)
408 406 404 402 400 398 396
Binding energy (eV)

Figure 4

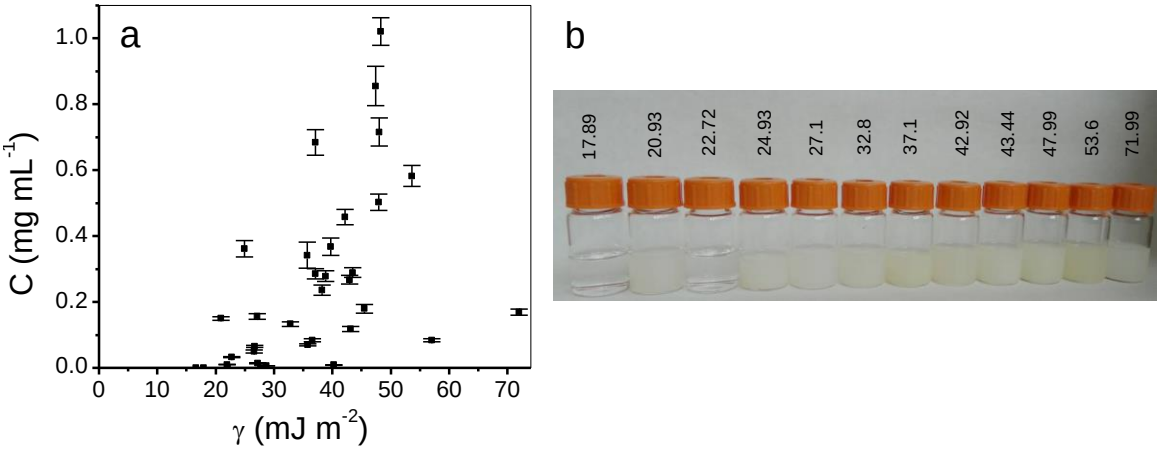
a
b
C (mg mL-1)
γ (mJ m-2)
0.0
0.2
0.4
0.6
0.8
1.0
0
10
20
30
40
50
60
70
17.89
20.93
22.72
24.93
27.1
32.8
37.1
42.92
43.44
47.99
53.6
71.99

Figure 5

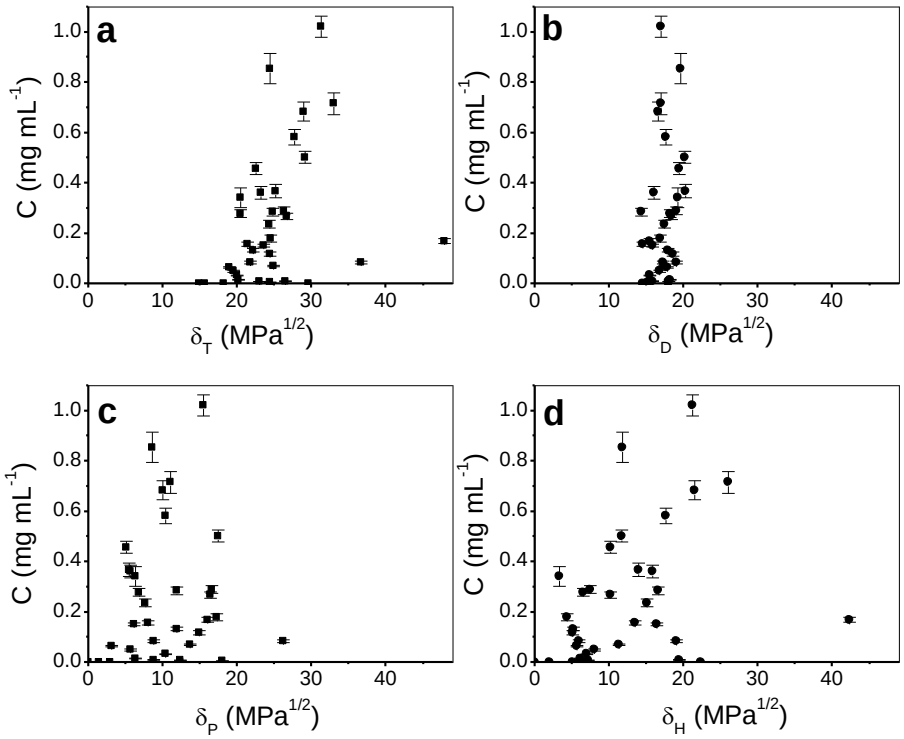
a
b
c
d
C (mg mL-1)
δT (MPa1/2)
δD (MPa1/2)
δP (MPa1/2)
δH (MPa1/2)
0.0
0.2
0.4
0.6
0.8
1.0
0
10
20
30
40

Figure 6

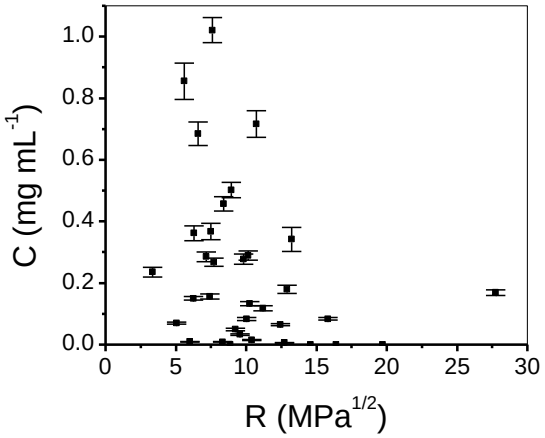

Figure 7

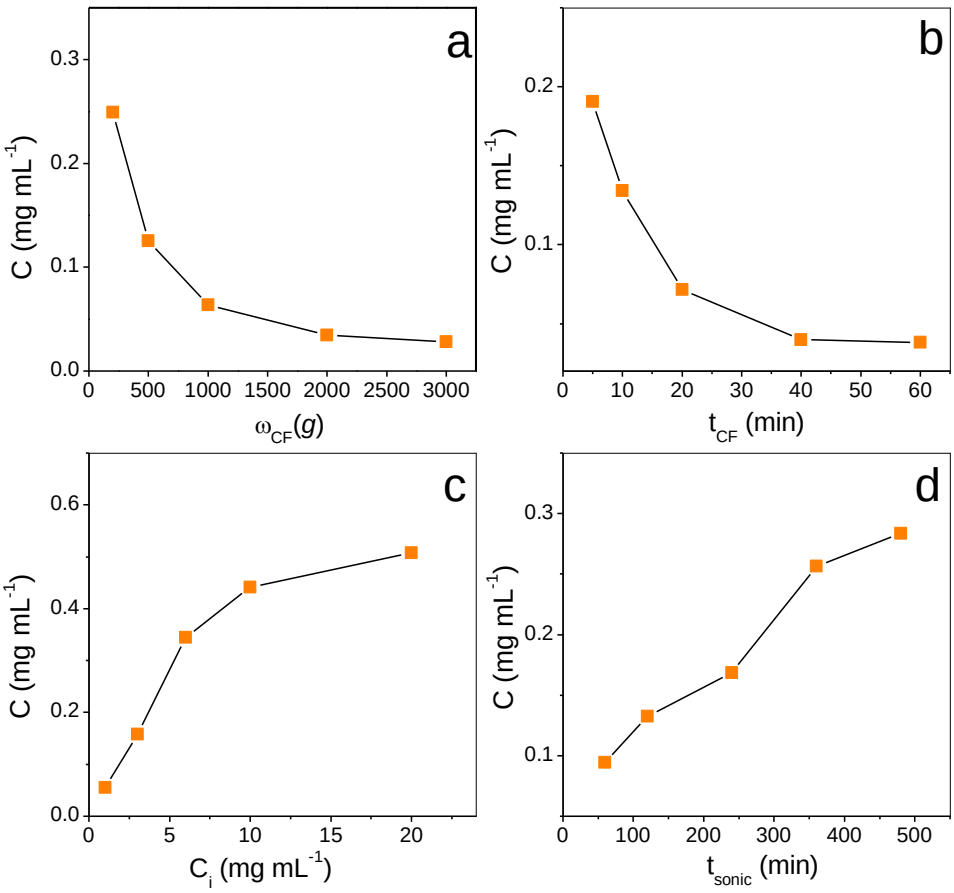

Figure 8

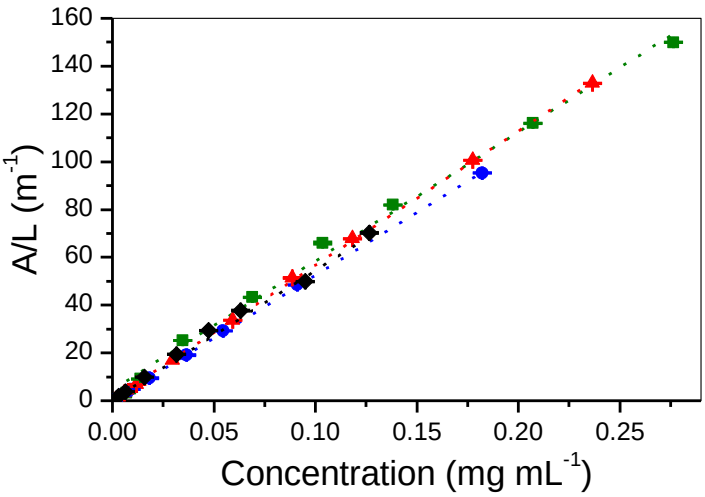
160
140
120
100
80
60
40
20
0
A/L (m-1)
0.00
0.05
0.10
0.15
0.20
0.25
Concentration (mg mL-1)

Figure 9

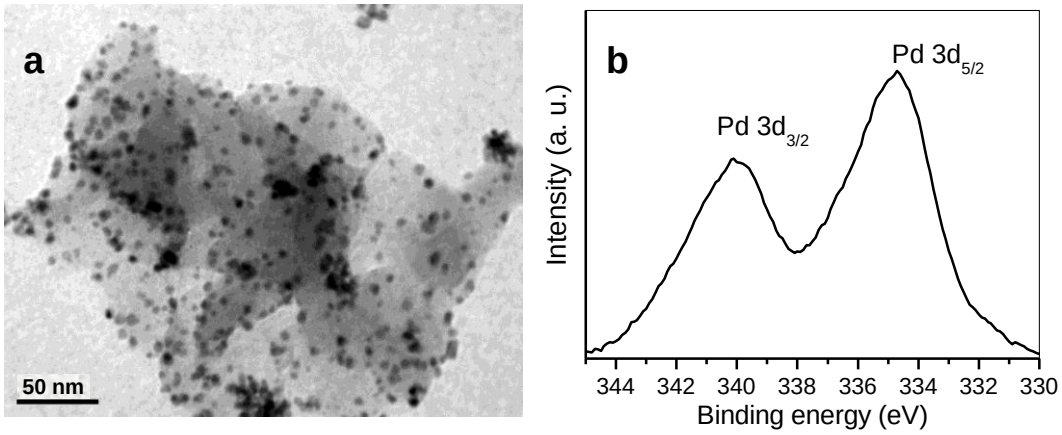
a
50 nm
b
Pd 3d5/2
Pd 3d3/2
Intensity (a. u.)
344
342
340
338
336
334
332
330
Binding energy (eV)

Figure 10

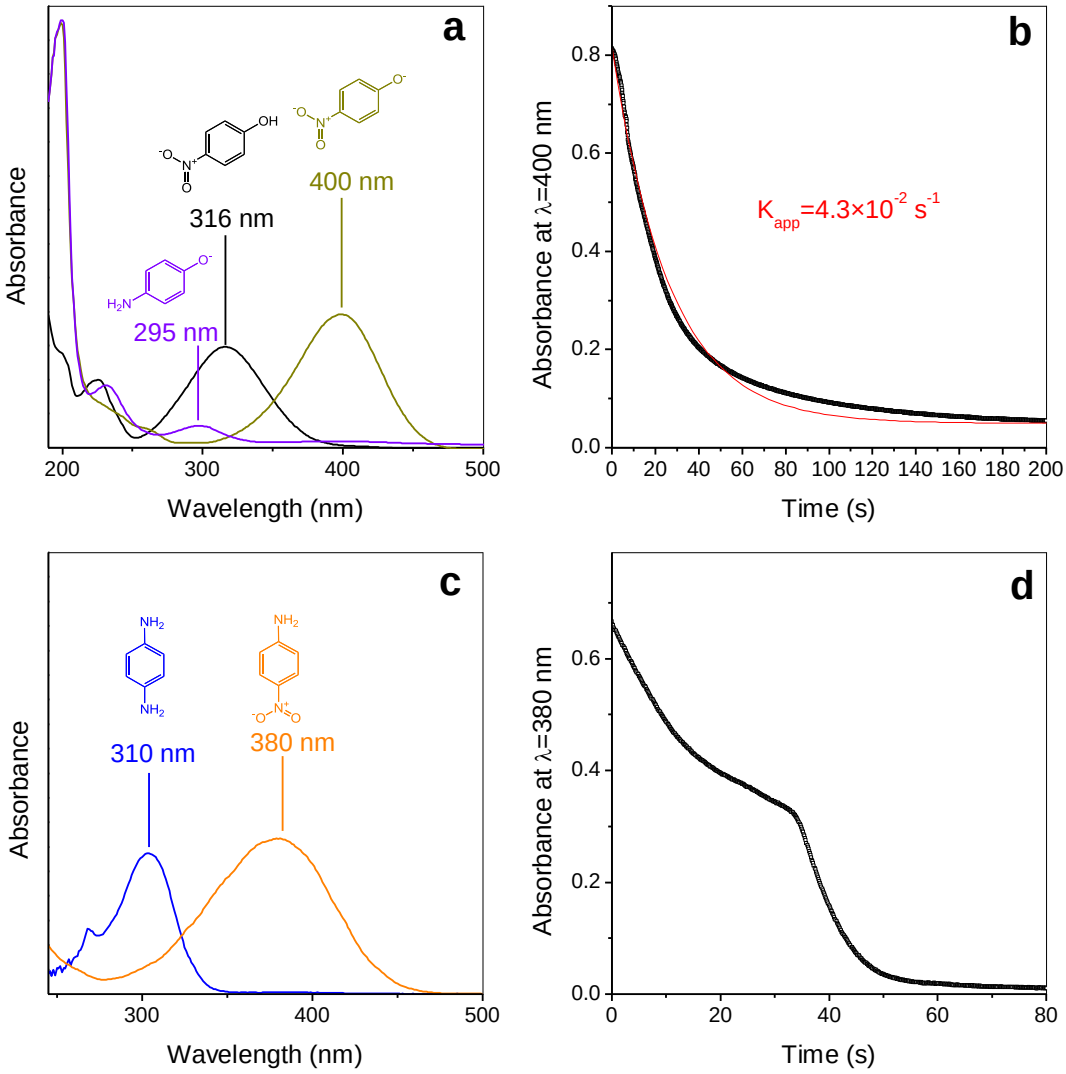
a
Absorbance
Wavelength (nm)
316 nm
400 nm
295 nm
200
300
400
500
b
Absorbance at λ=400 nm
Time (s)
K_{app}=4.3×10^{-2} s^{-1}
0.0
0.2
0.4
0.6
0.8
0
20
40
60
80
100
120
140
160
180
200
c
Absorbance
Wavelength (nm)
310 nm
380 nm
300
400
500
d
Absorbance at λ=380 nm
Time (s)
0.0
0.2
0.4
0.6
0
20
40
60
80

Figure 11

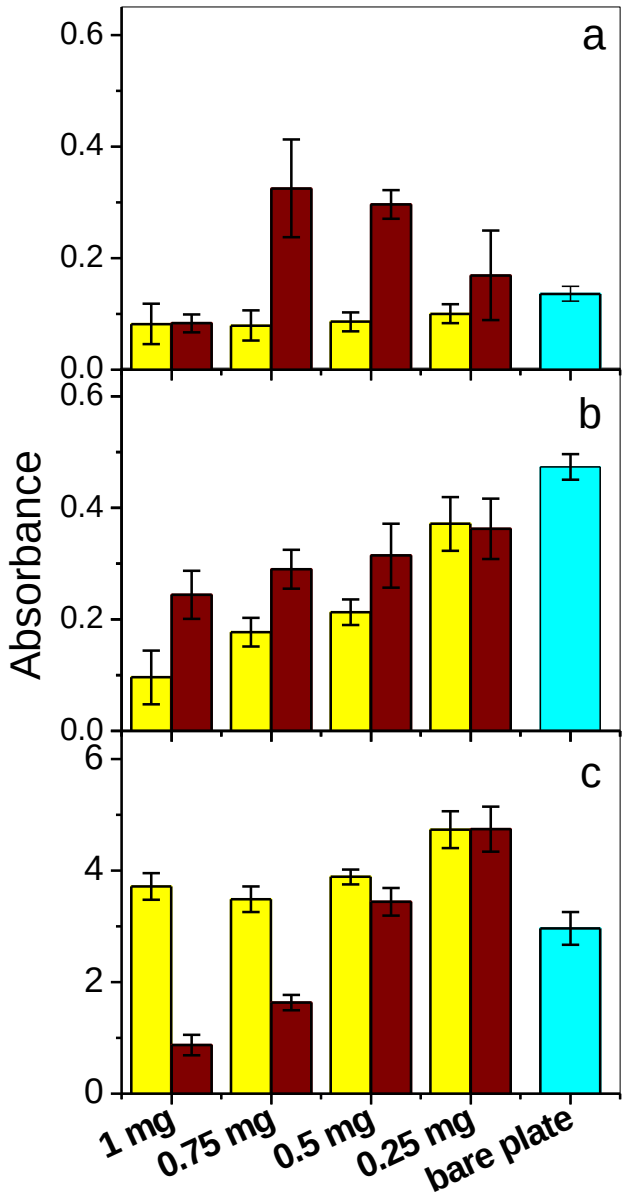
a
b
c
Absorbance
0.0
0.2
0.4
0.6
0
2
4
6
1 mg
0.75 mg
0.5 mg
0.25 mg
bare plate

Table of contents/Abstract graphic